LAMINAR LIQUID-LIQUID DISPERSION IN SMX STATIC MIXER

STUDY OF LIQUID-LIQUID DISPERSION OF HIGH VISCOSITY FLUIDS IN SMX STATIC MIXER IN THE LAMINAR REGIME

By

MAINAK DAS, B.Sc. Eng.

A Thesis

Submitted to the School of Graduate Studies

in Partial Fulfillment of the Requirements

for the Degree

Master of Applied Science

McMaster University

MASTER OF APPLIED SCIENCE (2011) McMaster University

(Chemical Engineering) Hamilton, Ontario

TITLE:	Study of Liquid-Liquid Dispersion of High Viscosity Fluids in SMX Static Mixer in the Laminar Regime
AUTHOR:	Mainak Das, B.Sc.Eng. (University of Alberta)
SUPERVISORS:	Dr. Andrew N. Hrymak and Dr. Malcolm H.I. Baird
NUMBER OF PAGES:	xiii, 67, A4, B3

Abstract

In this research, liquid-liquid dispersion of viscous fluids was studied in an SMX static mixer in the laminar regime. Backlighting technique was used for flow visualization, and the Hough transform for circle detection was used in OpenCV to automatically detect and measure drop diameters for obtaining the size distribution. Silicone oil and an aqueous solution of high fructose corn syrup were used for dispersed and continuous phases respectively, and sodium dodecyl sulfate was used as the surfactant to modify the interfacial tension. Experiments were conducted at varying viscosity ratios and flow rates-each at zero, low (~200 ppm) and high (~1000 ppm) surfactant concentrations. The effect of holdup was explored only for a few cases, but it was found to have a minimal effect on the weighted average diameter D_{43}.

It was found that the superficial velocity and the continuous phase viscosity had a dominant effect on D_{43}. The tail at the higher end of the droplet size distribution decreased with increasing superficial velocity and continuous phase viscosities. It was also found that D_{43} decreased with lowering of the interfacial tension. Furthermore, the effect of the dispersed phase viscosity was significant only at non zero surfactant concentrations.

An approximate model has been proposed that relates D_{43} to the capillary number. It is based on an energy analysis of the work done by the viscous and

surface forces on a drop of an initial diameter that is largely determined by the gap distance between the cross bars in the element.

Acknowledgements

I would like to sincerely express my gratitude to Dr. Hrymak and Dr. Baird for giving me this learning opportunity and guiding me throughout this project. Their commitment to the success of this research and innovative problem solving approaches has been truly inspirational.

I would like to thank Paul Gatt and Dan Wright for helping with equipment setup and troubleshooting. Their on-demand help made it possible to finish this project on time. I would also like to thank Justyna Derkach for providing guidance and assistance with lab safety.

My sincere thanks goes to Dr. Pelton`s group (especially Yuguo Cui) for providing access to their equipments. Also, I would like to thank my colleagues and friends for exchanging valuable information.

I would also like to acknowledge the financial support from the Department of Chemical Engineering and School of Graduate Studies by providing scholarships and teaching assistantships. I am also grateful to Proctor & Gamble for funding this project.

Lastly, I would like to thank my parents and other family members for their encouragement and constant support.

Table of Contents

Abstract iii

Acknowledgements v

Table of Contents vi

List of Figures viii

List of Tables xi

Nomenclature xii

1. Introduction 1

2. Literature Review 5

2.1 Drop breakup 5

2.2 Correlations in the laminar regime 11

2.3 Correlations in the turbulent regime 15

2.4 Automated droplet detection 19

3. Experimental 25

3.1 Fluids used 25

3.2 Experimental rig and procedure 26

3.3 Flow visualization setup and image capture 31

3.4 Image processing and circle detection 32

3.5 Note on measurement errors 38

4. Results and Discussion 40

4.1 D_{43} trends 40

4.2 D_{max} trends 47

4.3 Droplet size distribution trends 49

4.4 Qualitative Images 55

5. Conclusion 62

5.1 Summary 62

5.2 Recommendations for future work 64

References 65

Appendix A A1

Appendix B B1

List of Figures

Figure 1. Stability curves relating critical capillary number with the viscosity ratio 6

Figure 2. Critical Capillary number as a function of viscosity ratio for three different values of α 8

Figure 3. Drop breakup modes in shear flow 9

Figure 4. Break up modes 10

Figure 5. Effective shear rate for SMX and Kenics mixe 13

Figure 6. 3D parameter space in standard Hough Transform for circle detection 21

Figure 7. Two stage Hough transform illustration 22

Figure 8. Voting window 23

Figure 9. Process flow diagram with instrumentation 28

Figure 10. Entry configurations for continuous and dispersed phases 30

Figure 11. Flow visualization setup 32

Figure 12. Flow chart for image processing code 33

Figure 13. Sample raw image 34

Figure 14. Image after Bilateral Smoothing 35

Figure 15. Binary image after Canny Edge detection 36

Figure 16. Identified droplets 37

Figure 17. Log-log plot to show the effect of interfacial tension and viscosity ratio on D_{43} for μ_c ~25 mPaS 41

Figure 18. Log-log plot to show the effect of interfacial tension and viscosity ratio on D_{43} for μ_c ~70mPaS 42

Figure 19. Log-log plot to show the effect of interfacial tension and viscosity ratio on D_{43} for μ_c ~200 mPaS 42

Figure 20. Log-log plot to show the effect of viscosity ratio on D_{43} at zero surfactant concentration 44

Figure 21. Log-log plot to show the effect of viscosity ratio on D_{43} at low surfactant concentration 45

Figure 22. Log-log plot to show the effect of viscosity ratio on D_{43} at high surfactant concentration 45

Figure 23. Effect of number of elements on D_{43} 46

Figure 24. Effect of interfacial tension and viscosity ratio on D_{max} for μ_c ~25 mPaS 47

Figure 25. Effect of interfacial tension and viscosity ratio on D_{max} for μ_c ~70 mPaS 48

Figure 26. Effect of interfacial tension and viscosity ratio on D_{max} for μ_c ~200 mPaS 48

Figure 27. Image showing the breakup of a dispersed phase stream into drops as it is passes through the gap between the cross bars 56

Figure 28. Image sequence showing drop breakup from impact with cross-points of the packing 56

Figure 29. Image sequence showing a single drop breakup at cross-point 57

Figure 30. Model assessment by correlating D_{43} with capillary number 60

List of Tables

Table 1. Correlations for droplet diameter in static mixers in the turbulent regime 18

Table 2. Properties of fluids used in experiments 25

Table 3. Relative errors of measured and calculated values 38

Table 4. Droplet size distribution trends at zero surfactant concentration 50

Table 5. Droplet Size Distribution Trends at High Surfactant Concentration 53

Nomenclature

Ca	capillary number
Ca_{crit}	critical capillary number
CoV	coefficient of variation
D	mixer diameter, m
D_0	drop primary diameter, m
D^{16}	diameter below which 16% of the droplets lie in a distribution, m
D_{32}	sauter mean diameter, m
D_{43}	volume mean diameter, m
D^{84}	diameter below which 84% of the droplets lie in a distribution, m
D^{90}	diameter below which 90% of the droplets lie in a distribution, m
D_f	final droplet diameter after breakup of a primary drop, m
D_i	diameter of an individual drop in a distribution, m
D_{max}	maximum diameter, m
E	overall energy, J
L_T	large turbulence scale, m
N	number of droplets formed after break
n	number of mixing elements
N_0	number of droplets with an initial diameter D_0
p	viscosity ratio (dispersed to continuous phase)
Q	volumetric flow rate, m^3/s
r	drop radius, m

Re Reynolds number

u superficial velocity, m/s

Vi viscosity group

Vol_{mixer} mixer volume, m^3

We Weber number

ΔP pressure drop across the mixer, Pa

Greek Letters

$\dot{\gamma}$ shear rate, s^{-1}

α flow parameter

ε power dissipation per unit mass, m^2/s^3

ϕ dispersed phase volume fraction

η Kolmogorov scale, m

μ viscosity, Pa.S

ρ density, kg/m^3

σ interfacial tension, N/m

τ shear stress, Pa

Subscripts

c continuous phase

d dispersed phase

e emulsion

h hydraulic

p pore

1. Introduction

Motionless mixers or static mixers have been in use since the 1970's (Thakur et al., 2003), and with time they have evolved to the point where they are now found in a wide array of industries. These range from grain processing, pharmaceuticals and cosmetics to petrochemicals, refining, and specialty chemicals. They are used in continuous processes in both distributive and dispersive mixing applications. In general static mixers are more energy efficient, and among other applications, they are used instead of continuous stirred tanks with rotating impellers for systems with relatively short residence times, plug flow conditions and for blending or dispersing fluids that are sensitive to high shear. They also become a more cost effective option for high pressure services. These benefits are realized because of a static mixer's mechanical simplicity and compactness.

A typical static mixer contains a series of mechanical inserts- the number, type and sequence of which are chosen to suit a particular application and to optimize the mixing performance. These inserts can be broadly categorized to have twisted- ribbon, plate and structured geometries. The twisted-ribbon type is the earliest of static mixer internals, and is ideal for distributive mixing of low viscosity fluids (such as gas-liquid dispersions) under turbulent conditions. Plate type mixers are also used for applications in the turbulent flow regime, as these

designs create vortices. Structured packings have more complex geometry and are often placed such that each cartridge is oriented 90^0 relative to its neighbours. The most versatile in this category are the SMX (Sulzer, USA) and SMXL, which have geometries with cross bars angled at 45^0 and 30^0 for SMX and SMXL respectively. SMX- which is the subject of study in this thesis-is regarded to be the best design choice for plug flow in tubular reactors, and for blending and dispersing high viscosity fluids in the laminar flow regime (Paul et al., 2004, p. 428).

In order to scale up static mixers reliably in liquid-liquid dispersion applications, it is of prime importance to develop correlations or fundamental models to predict key characteristics such as pressure drop, mean droplet size and size distributions. The latter two are applicable to multi phase flow, which complicates fluid dynamic studies because of fluid properties of multiple phases, which includes interfacial tension. Such correlations and fundamental insights also help to optimize the packing geometry for better performance. In liquid-liquid dispersions with SMX packing for example, there is a strong drive from the industry to eliminate the occurrence of oversized droplets in order to produce a more uniform or narrower droplet size distribution. An appreciable amount of numerical and experimental work has been done in this area, since the fundamental contribution by Grace (1982). For example, Rauliene et al. (1998) have done numerical investigations to characterize the extent of elongation flow

in various static mixers. Liu (2005) has done numerical and experimental studies to study flow fields inside an SMX mixer. He also conducted numerical simulations and experimental validations for single drop breakup in the laminar regime (Liu et al., 2005). Direct investigations of droplet size distribution in SMX mixers have been done by Legnard et al.(2001), Rao et al. (2007), Fradette et al.(2007), Theron et al.(2010) and Das et al.(2005). Legnard and Felice studied droplet dispersion in the turbulent regime and have based their correlations on the classical Kolmogorov theory, whereas Fradette , Das and Rao have studied it in the laminar regime. In all these studies, a major limiting factor was the measurement of droplet size distribution. In most cases the measurement was done using the micro encapsulation technique where the droplets were hardened at the surface by means of interfacial polymerization. Rao et al. (2007) and Fradette et al. (2007) used image/video capture and then manually counted and measured the droplets to obtain a distribution. The latter technique, because of the detailed measurements involved, imposes serious limitations on the amount of data that can be acquired. Automating this process with computer vision algorithms would have certainly helped the experimenters to conduct more runs under different conditions, and come up with better correlations.

The research objective in this thesis is therefore is twofold. The first part will be to leverage computer vision algorithms for automation and explore their merits for rapid measurement of Droplet Size Distribution (DSD). The second

part will be to collect substantial data with the SMX elements in the laminar regime under varying viscosity ratios, holdups and most importantly under varying interfacial tension. Finally, this data will be used to study Droplet Size Distribution (DSD) trends and to develop a model for correlating the variables involved.

2. Literature Review

2.1 Drop breakup

In order to understand liquid-liquid dispersions in a mixer it is important to understand the physics of drop breakup. Different breakup mechanisms under different conditions can affect the maximum drop size and the nature of the size distribution in a dispersion. The corollary of this fact is that the identification of different size distributions (such as Gaussian, Log-normal, bimodal etc) in a relatively less understood equipment can give an insight into the flow conditions or breakup modes inside it.

A drop can break up as a result of the hydrodynamic forces around the drop and/or as a result of collision with the internals of the mixer. When it breaks up because of the hydrodynamic forces, the viscous shear stress from the continuous phase exceeds the drop's internal viscous and surface stresses. Grace (1982) has done fundamental work in this regard with single drop breakup experiments in steady simple shear and 2D extensional flow. He was able to describe the breakup in terms of two dimensionless terms namely the capillary number and the viscosity ratio. The capillary number in this case is defined as

$$Ca = \frac{\mu_c \dot{\gamma} r}{\sigma} \tag{1}$$

where $\dot{\gamma}$ is the shear rate and r is the radius of the drop. This definition is also synonymous with reduced shear rate (dimensionless shear rate). The viscosity ratio is defined as the ratio of the dispersed phase viscosity to the continuous phase viscosity and is given as

$$p = \frac{\mu_d}{\mu_c} \tag{2}$$

Figure 1 shows the relationship between the critical capillary number and viscosity ratio

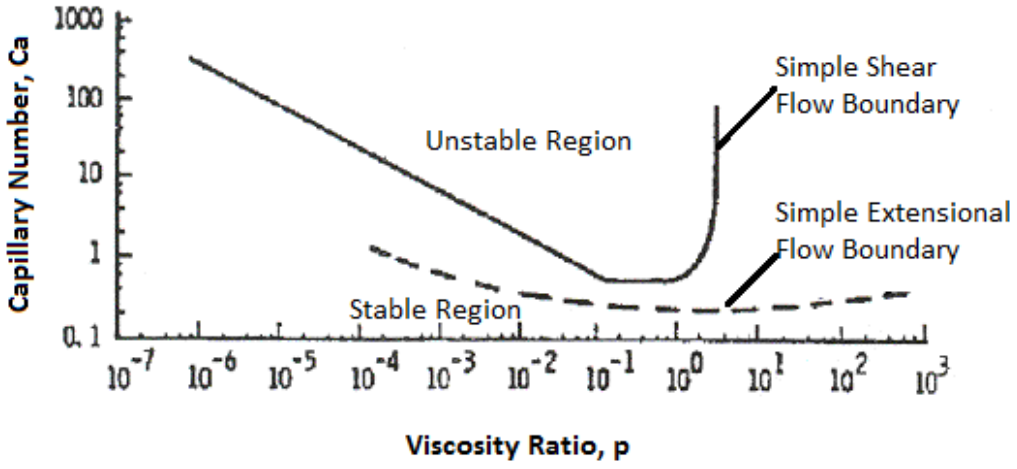

Figure 1. Stability curves relating critical capillary number with the viscosity ratio (data from Grace, 1982)

The drops break up when the capillary number exceeds a critical value. It can be seen that for extensional flow the critical values are far lower than those of simple shear, thus signifying that extensional flow is more efficient in breaking

drops. Depending on the mixer geometry, any degree of simple shear to elongation flow is realizable. This is quantified by a flow parameter α, which is defined as the ratio of the deformation (strain rate) to the rotational (vorticity) component of the flow field and is given as

$$\frac{magnitude\ of\ strain\ rate}{magnitude\ of\ vorticity} = \frac{1+\alpha}{1-\alpha} \tag{3}$$

α=0 for simple shear and α=1 for purely extensional flow. Bentley and Leal (1986) have used a computer controlled four roll mill to generate different types of two dimensional flow. By being able to control the direction and speed of the four rollers, they were able to set a desired ratio of the strain rate to the vorticity components of the flow field in between the rollers, thereby producing intermediary values of α (between zero and one). Figure 2 shows the critical capillary curves for values of α=0 (purely extensional), α=0.2, α=1 (simple shear)

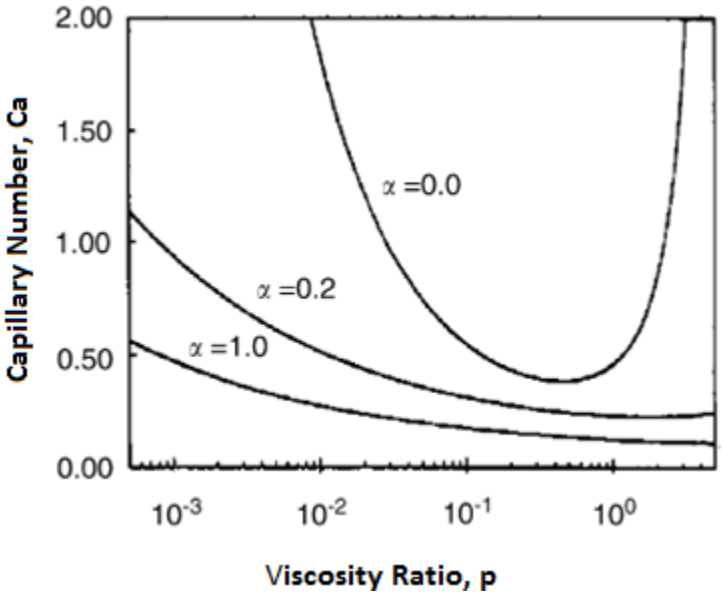

Figure 2. Critical Capillary number as a function of viscosity ratio for three different values of α (after data Bentley and Leal ,1986)

It is also important to consider the effects of breakup in transient conditions. Rauline et.al (1998) has shown with his numerical investigation that the flow parameter α changes along the length of a SMX static mixer. Hence a drop experiences a transient flow field inside the mixer. Stone and Leal (1989) studied the effects of transient conditions and found that by combining and altering the flow types the drop can break at capillary numbers which are lower than the critical values at steady conditions.

The modes of drop breakup depend on the viscosity ratio, surfactant concentration, capillary number and flow conditions. The four typical modes are necking, tip streaming, end-pinching and capillary instability. Figure 3 shows where some of these modes occur in a simple shear flow

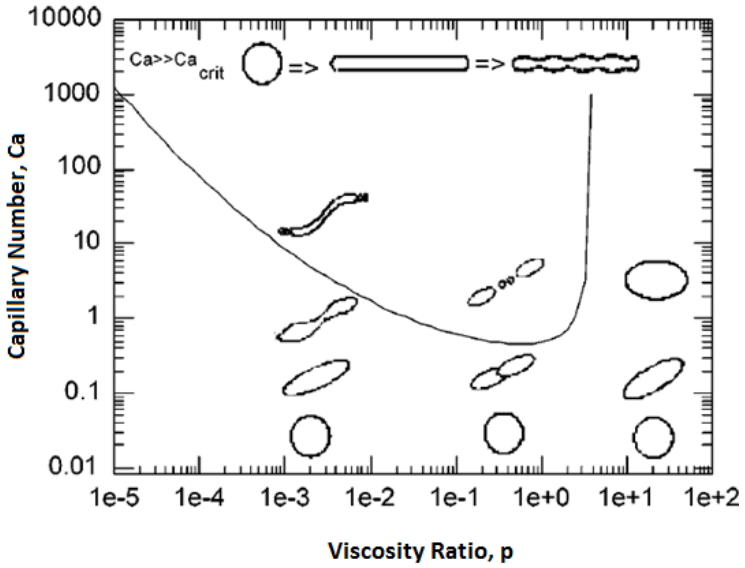

Figure 3. Drop breakup modes in shear flow (from Tucker and Moldenaers, 2003)

When the viscosity ratio, p is ≈1, the drop narrows at the center, assumes a dumbbell shape and ultimately breaks into two mother drops with a few daughters in between. Tip streaming occurs when p<1, and daughter droplets are released from the tips. This type of breakup typically gives rise to a log-normal distribution. When the capillary number far exceeds the critical value the drop stretches, orients itself in the direction of the flow and breaks up because of capillary wave instability. The effect of surfactant concentration on breakup modes has been mentioned in Jansen (1997) and is shown in Figure 4. At low surfactant concentrations, necking is predominant whereas tip streaming occurs with higher surfactant concentration. This is because interfacial tension gradients develop that cause unequal distribution of surface forces (de Bruijin, 1993).

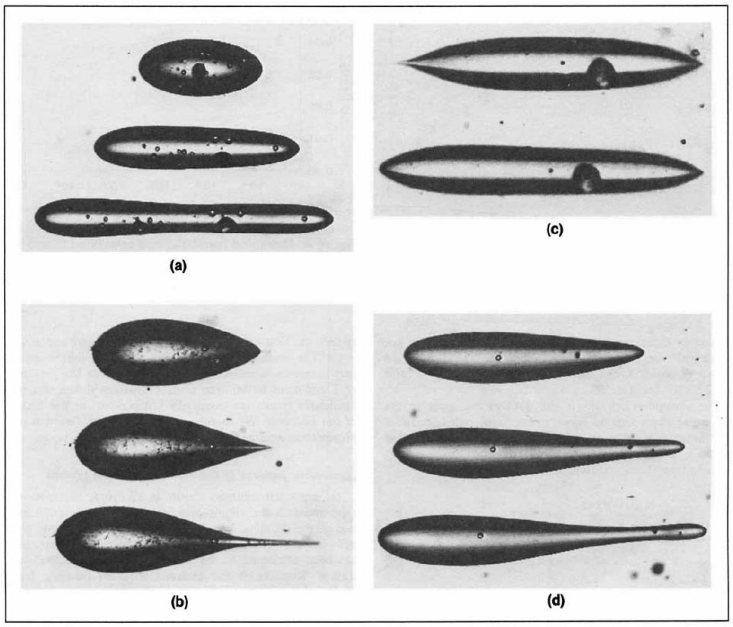

Figure 4. Break up modes-a)narrowing waist breakup (no surfactant) b) one sided elongation (low-moderate surfactant conc.) c) narrowing waist with tip streaming (low surfactant conc.) d) highly-asymmetric narrowing waist breakup (high surfactant conc.) (from Jansen, 1997)

Correlations of drop sizes in a liquid-liquid dispersion are usually done in terms of the Sauter mean diameter, and is particularly useful when interfacial mass transfer is being considered. The Sauter diameter is the ratio of the third to second moment of the distribution and is given by

$$D_{32} = \frac{\sum_{i=1}^{m} n_i {D_i}^3}{\sum_{i=1}^{m} n_i {D_i}^2} \tag{4}$$

The measure D_{43} is also used in some correlations. It is the ratio of the fourth to the third moments, and is referred to as the *mass mean diameter*. It is given by

$$D_{43} = \frac{\sum_{i=1}^{m} n_i {D_i}^4}{\sum_{i=1}^{m} n_i {D_i}^3} \tag{5}$$

D_{43} places more emphasis on the larger drop sizes in the distribution. There are also other measures such as D^{90}, which is the diameter greater than 90% of the droplets in a sample.

Other correlations are given in terms of coefficient of variation or CoV. It is defined as the ratio of standard deviation to the mean of a sample size. It gives an indication of the spread of the DSD. For a Gaussian distribution, which can be inferred from a straight line in a cumulative frequency plot (Paul et al. 2004, pg. 677), the CoV is given as

$$CoV = \frac{D^{84} - D^{16}}{2D^{50}} \tag{6}$$

where D^{84}, D^{16} and D^{50} are defined similarly as D^{90}.

2.2 Correlations in the laminar regime

There have been a few experimental studies in dispersion with SMX static mixer in the laminar regime. Streiff (1997) has obtained correlations to predict maximum diameter (dmax) for viscosity ratio, p<1, in the laminar regime. He correlated the critical capillary number with the relation-

$$Ca_{crit} = 0.1p^{-1/6} \tag{7}$$

D_{max} can then be estimated from the definition of the capillary number-

$$D_{max} = Ca_{crit}\frac{2\sigma}{\dot{\gamma}\mu_c} \tag{8}$$

The above equation is valid when the drop residence time in the mixer is twenty times greater than the critical burst time obtained by Grace (1982) in 2D extensional flow. The critical burst time is the minimum time that is needed to sustain the critical shear rate (calculated using Ca_{crit} from Fig. 1) for drop breakup.

Fradette (2007) has done systematic experiments to study the effects of dispersed phase concentration, number of elements and the energy input on the average diameter. It was found –albeit with limited data-that the average drop size varied exponentially as $D_{avg} \propto e^{2.3\emptyset}$, and with the viscosity ratio with the relation $D_{avg} \propto p^{-0.06}$, where D_{avg} is the mean of the distribution when plotted with logarithm of the diameter as the random variable. The viscosity ratio ranged between 5-200, and the dispersed phase concentration (or holdup) - defined as

$$\emptyset = \frac{u_d}{u_c + u_d} \tag{9}$$

ranged from 5-25%. Furthermore, to characterize the performance of SMX mixer, the effective shear rate -given as

$$\dot{\gamma}_{eff} = Ca_{crit}\frac{\sigma}{(D/2)}\mu_c \tag{10}$$

-was compared (shown in Figure 5) and was found to be higher than that of Kenics mixer for a given overall energy (Karbstein and Schubert, 2005)given by

$$E = \Delta P Vol_{mixer} \tag{11}$$

where ΔP is the pressure drop in the mixer and V_{mixer} is the total volume of the mixer. The critical capillary number, Ca_{crit}, in Eq (10) is assumed to be constant and is obtained from the chart for extensional flow given in Figure 2. It was assumed constant because flow within SMX was largely assumed to be of the extensional type. This assumption is however, not accurate as shown by experiments in Liu (2005).

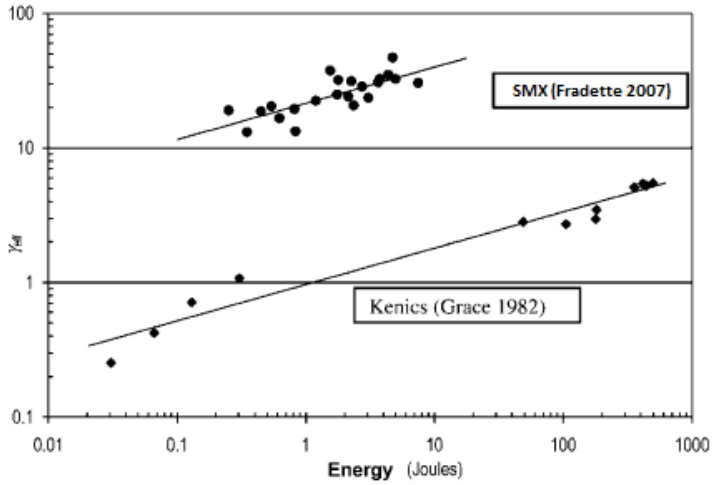

Figure 5. Effective shear rate for SMX and Kenics mixer (from Fradette, 2007)

The approach of Das et al. (2004) was to treat elements of the mixer as a bundle of narrow pores. The drop breakage was assumed to occur in the boundary layer within the pore with a strain rate of

$$\dot{\gamma} = 4u_p/D_p \tag{12}$$

where u_p is the average velocity in the pore and D_p is the pore diameter. With appropriate choice of D_p and u_p, and with an assumed critical capillary number, the droplet diameter (maximum stable diameter) could be estimated using non-dimensionless terms :

$$\frac{D_{max}}{D_p} = \frac{2Ca_{crit}}{Vi_p} \tag{13}$$

where Vi_p is the pore viscosity number defined as

$$Vi_p = \frac{\mu_e u_p}{\sigma} \tag{14}$$

The emulsion viscosity (μ_e) is considered here instead of the continuous phase viscosity, and is a function of the dispersed phase fraction. The change in apparent viscosity of the continuous phase has also been observed by Fradette (2007). With a similar approach, another equation was derived for intermediate Reynolds number($20<Re_p<350$) by considering the inertial forces that-unlike in laminar creeping flow- were assumed to have dominance over the viscous shear forces The relation in this case was derived as-

$$\frac{D_{max}}{D_p} \alpha \, We_p{}^{-0.33} \tag{15}$$

where We_p is the pore Weber number. Experimental data collected to validate the above models were limited , showed some scatter , and also deviated from values as predicted by the models.

Rao et.al (2004) derived a model assuming that a small drop would collide and attach to the packing and grow until the drag forces from the continuous phase would become large enough to detach it. The model is shown in the equation below-

$$\frac{D_{43}}{D} = k_d[1.5\emptyset(1+p)]^{1/2} \tag{16}$$

where k_d is a constant. The inertial and surface forces were considered to be negligible. The model might be of relevance in a situation where the dispersed phase wets the packing material.

2.3 Correlations in the turbulent regime

Many droplet size correlations have been developed for the turbulent regime in SMX static mixers. They are based on Kolmogorov theory of isotropic turbulence. A droplet is assumed to breakup in eddies with length scales smaller than the droplet diameter. These scales are somewhere in between the large (primary) turbulence scale and the Kolmogorov microscale (Paul et al., 2004, pg. 657), given by

$$\eta = \left(\frac{\mu_c}{\rho_c \epsilon}\right)^{1/4} \tag{17}$$

where ε is the power dissipation per unit mass. The energy spectrum density in this range is given by

$$E(k) = \frac{3}{2}\epsilon^{2/3}k^{-5/3} \;\; (L_T \gg d \gg \eta) \tag{18}$$

The shear stress to break up the drop is given by

$$\tau_c = \rho_c \int_{1/d}^{\infty} E(k)dk \approx \rho_c \varepsilon^{2/3} d^{2/3} \tag{19}$$

for low dispersed phase viscosities, this result translates to the following relation

$$D_{max} \propto \left(\frac{\sigma}{\rho_c}\right)^{3/5} {\epsilon_{avg}}^{-2/5} \tag{20}$$

where,

$$\epsilon_{avg} = \frac{Q\Delta P}{Vol_{mixer}\rho_c} \tag{21}$$

The above relation is equivalent to

$$\frac{D_{max}}{D} \propto We^{-0.6} \tag{22}$$

where We is the Weber number-a dimensionless number, which is a ratio of the inertial to surface forces. Most correlations in the turbulent regime are based on Eq (22), and have been modified to account for dispersed phase viscosity, friction factor (Middleman, 1974), number of elements etc. These correlations have

been summarized for Kenics and SMX mixers in Table 1. Middleman (1974), Berkman and Calabrese (1988), and Theron et al. (2010), have used the superficial velocity, and hence the Weber number in their correlations is given as-

$$We_c = \frac{\rho_c u_c D}{\sigma} \tag{23}$$

Streiff et al. (1997) used a hydraulic diameter and interstitial velocity instead of the mixer diameter and superficial velocity. Legnard et al. (2001) used a pore diameter and pore superficial velocity, by considering the mixer elements as a bundle of cylindrical pores. Both the hydraulic and pore diameters are dependent on the type of the mixer. The Weber numbers We_h and We_c, are defined analogously to Eq (23). Furthermore, to take into account the dispersed phase viscosity μ_d, Berkman and Calabrese (1988) have introduced the viscosity group given as

$$Vi = \frac{\mu_c u_c}{\sigma}\left(\frac{\rho_c}{\rho_d}\right)^{0.5} \tag{24}$$

Table 1. Correlations for droplet diameter in static mixers in the turbulent regime

Author	Mixer Type	Correlation	Dispersed phase vol. fraction range
Middleman (1974)	Kenics	$\frac{D_{32}}{D} = K_4 {We_c}^{-0.6} Re^{0.1}$	$0.005 \leq \emptyset \leq 0.01$
Streiff et al. (1977)	SMV	$\frac{D_{32}}{D_h} = 0.21 {We_h}^{-0.5} {Re_h}^{0.15}$	$\emptyset \leq 0.25$
Berkman and Calabrese (1988)	Kenics	$\frac{D_{32}}{D} = 0.49 {We_c}^{-0.6} \left(1 + 1.38 Vi \left(\frac{D_{32}}{D}\right)^{0.33}\right)^{0.6}$	$0.05 \leq \emptyset \leq 0.25$
Legnard et al. (2001)	SMX	$\frac{D_{32}}{D_p} = 0.29 {We_p}^{-0.2} {Re_p}^{-0.16}$	$\emptyset \leq 0.1$
Theron et al. (2010)	SMX	$\frac{D_{32}}{D} = 0.15 {We_c}^{-0.6} {Re_c}^{0.1} n^{-0.2}$, $n \leq 10$ is the number of elements	$\emptyset \leq 0.25$

2.4 Automated droplet detection and measurement

There are two classes of algorithms for pattern recognition in an image: local and global processing methods. Local processing algorithms look for patterns in a specified area of an image, whereas in global approaches, the entire image is considered at a time to detect shapes or patterns. In one type of local processing algorithm for example, an edge pixel (discontinuity in brightness intensity) in a binary image is linked with adjacent pixels with pre-defined criteria. Such a method was used by Kim and Lee (1990) to detect and measure droplets from a spray nozzle. Pixels were grouped together based on rules, and classified (based on simple patterns) either as potential drops or foreign objects. The group of connected pixels were then measured for the diameter. One major drawback of their algorithm is that it is incapable of detecting overlapping drops, and is very sensitive to noise-in the binary image.

The Hough Transform (Bradski and Kaehler, 2008, pg. 153) is a global processing algorithm, which has been gaining popularity for line and circle detection applications. It has been used in disciplines ranging from oceanography to microbiology, and is also used for pupil/iris detection and tracking. It has an advantage over other algorithms because it can detect and measure circles simultaneously, is capable of detecting overlapping circles and is more robust for noisy images. In essence, it is a voting algorithm whereby an edge pixel in a binary image is used to vote for all possible circles or lines that it

could belong to. To illustrate this, we consider a circle represented by the equation

$$(x-a)^2 + (y-b)^2 = r^2 \tag{25}$$

where the coordinates of the centre (a,b) and the radius r, are parameters that completely define the circle. An edge pixel can therefore be used to compute all possible (a,b,r) values in the parameter space, and vote for these parameter triplets in a 3D accumulator array. A ``vote`` is typically implemented by incrementing the value in the cell of the array by one. From a geometrical standpoint, the standard Hough transform algorithm votes for all the points on a right circular cone that emanates from the edge pixel. The concept is schematically shown in Figure 6. If a set of edge pixels are indeed a part of a circle, then the parameters (a,b,r) corresponding to that circle will receive more votes than its neighbouring points in the 3D accumulator array. The final step in the algorithm is therefore to find local maxima in the accumulator array and mark detected circles.

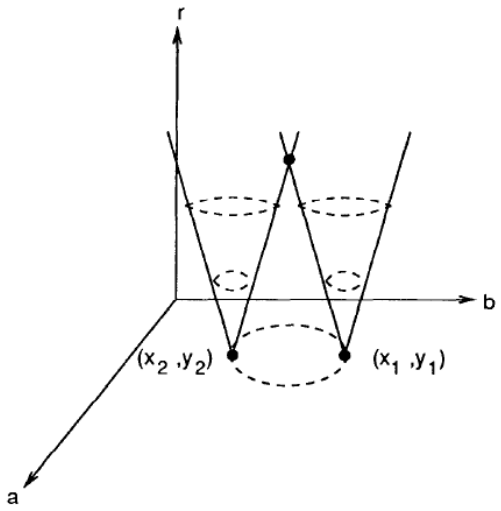

Figure 6. 3D parameter space in standard Hough Transform for circle detection (from Yuen et al. 1990)

This standard Hough transform algorithm has an inherent disadvantage because the 3D accumulator array demands more memory and also computational time for searching for local peaks within it. Furthermore, the accumulator grows only larger as the range of radii increases.

Many optimized versions of this algorithm have been developed to increase the computational efficiency. Yuen et al. (1990) did a comparative study on different variants of the algorithm, and concluded that the Gerig Hough Transform with gradient (GHTG) and 2 stage Hough transform (2HT) have the best combination of accuracy and efficiency. 2HT has been adopted in standard freely available libraries such as OpenCV. In the first stage of 2HT, the voting is done only along the direction of the edge gradient. This requires only a 2D accumulator array, and because the centre of a circle lies along the direction of the gradient, the centres are found by finding the local maxima in the

accumulator array. In the second stage, for each centre found, distances to edge pixels within a specified radius are computed. A radius histogram is then constructed for that candidate centre, wherein a peak would identify the most probable radius . The pictorial representation of 2 HT is shown in figure 7.

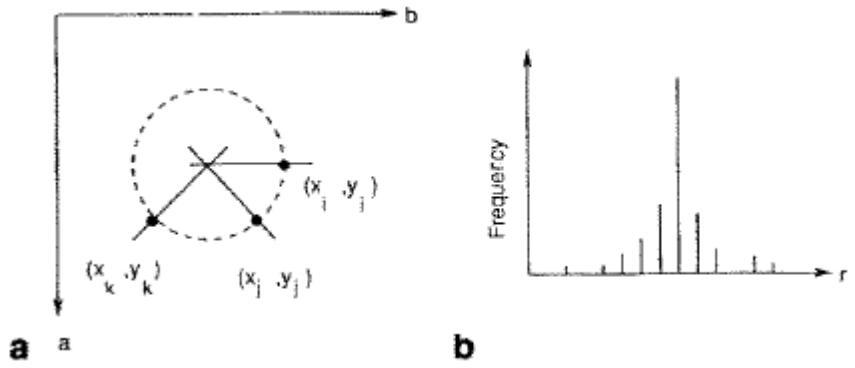

Figure 7 a) first stage 2D accumulator array to find centres b) histogram for a given candidate centre to find the radius in the second stage (from Yuen et al. 1990)

The Hough transform has been used very recently by Bras et al. (2009) to automate DSD measurement for liquid-liquid dispersions in a stirred mixer/settler device. To reduce the number of noise votes, the edge gradient information was also used to vote in only two sections of the right circular cone in the 3D accumulator. This is shown in Figure 8.

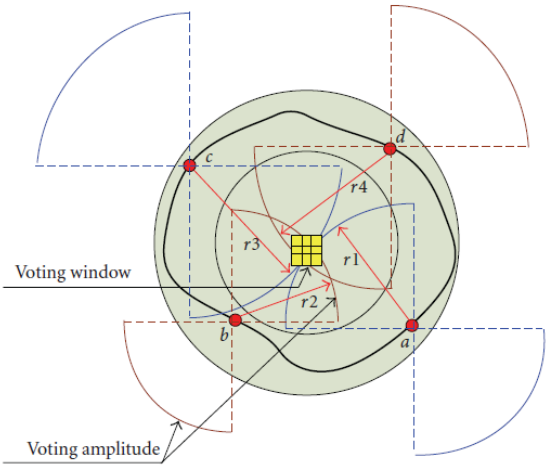

Figure 8 Voting window (Bras et al., 2009)

Brás et al. (2009) also found that the algorithm is susceptible to detecting false droplets when the image quality is poor. This is because poor quality images can cause more noisy edges (erroneously detected edges), which results in more noise votes. It also leads to erroneous computations of edge gradient directions. Therefore, to quantify the performance of the algorithm they used two metrics, which are defined as follows-

$$recall = \frac{TP}{TP + FN} \tag{26}$$

$$precision = \frac{TP}{TP + FP} \tag{27}$$

where TP, FP and FN stand for true positives, false positive and false negatives respectively. In an ideal case both recall and precision should be 100 %. However, in a typical case there is a trade off between these two metrics. Bras et al. (2009), saw their recall and precision varying from 90% to 50 % , depending

on the quality of the image. Hence, while using this algorithm it is imperative that the drops in the image be in sharp focus with minimal motion blur.

3. Experimental

3.1 Fluids used

Silicone oil was used as the dispersed phase and an aqueous solution of High Fructose Corn Syrup (HFCS) was used for the continuous phase. The silicone oil used was Xiameter-PMX200 silicone fluids from Dow Corning, and the HFCS was supplied by UNIVAR Canada. The properties of the fluids are given in Table 2. Because of limited accuracy in measuring large volumes, and due to the non linear behaviour of HFCS viscosity with dilution, it was difficult to prepare an exact HFCS solution. Hence the actual viscosities were measured every time after a HFCS solution was prepared. They differed slightly with the values given in table 2, and have been included in the data table in appendix A. The viscosity was measured by the Brookfield Viscometer (using spindle #1) and verified with Zahn Cups measurements. All viscosity measurements were carried out at room temperature of 21^0C.

Table 2. Properties of fluids used in experiments

	HFCS Soln. (90%)	HFCS Soln. (80%)	HFCS Soln. (70%)	Silicone Oil (500 CSt.)	Silicone Oil (1000 CSt.)
density[3] (kg/m3)	1360	1320	1280	978	978
viscosity (mPaS)	200	70	25	489	978

Sodium dodecyl sulphate (SDS) was used as the surfactant, to lower the interfacial tension. The critical micelle concentration (CMC) of SDS in pure water

at 25^0C is 0.0082 M (Mukherjee and Mysels, 1971), which corresponds to 2365 ppm. The experiments were carried out below this concentration-starting from zero, low (~200 ppm), and then finally at high (~ 1000 ppm) concentration levels. The interfacial tensions corresponding to these three levels were 40, 20 and 12 mN/m respectively. A fresh batch of HFCS solution was made between each surfactant concentration level. The actual interfacial tension was measured for every batch after surfactant addition to ensure that it was close to the aforementioned values.

The interfacial tension measurements were done using the pendant drop method with the DSA10 unit from Kruss, Germany. This device is typically used to measure the surface tension at the liquid-air interface. However, in this case the interfacial tension at the liquid-liquid interface was measured using a transparent acrylic cuvette, which was filled with silicone oil. The heavier HFCS solution was used for the drop phase, and the drop was created inside the surrounding silicone oil. Since the cuvette was transparent, the drops were imaged and the interfacial tension values were reported by the software based on the analysis of the drop shape.

3.2 Experimental rig and procedure

A schematic of the experimental rig with relevant instrumentation is shown in figure 9. The static mixer used is made of acrylic, and is surrounded by

a mineral-oil filled light box to correct for the refractive distortion caused by the curvature of the inner cylindrical surface. The mixer's inner diameter is 41.18 mm and its height is 92 cm. A smaller mixer with a diameter of 15.75 mm was also used, but because of time constraints only limited runs were obtained. Plastic shims support the SMX inserts which fit snugly inside the column. These SMX elements are made of titanium and have the same geometry as described in Rao et. al (2007). They have a L/D ratio of one with a void fraction of 0.892, and are arranged in the conventional form with each element oriented 90^{o} with respect to its adjacent ones.

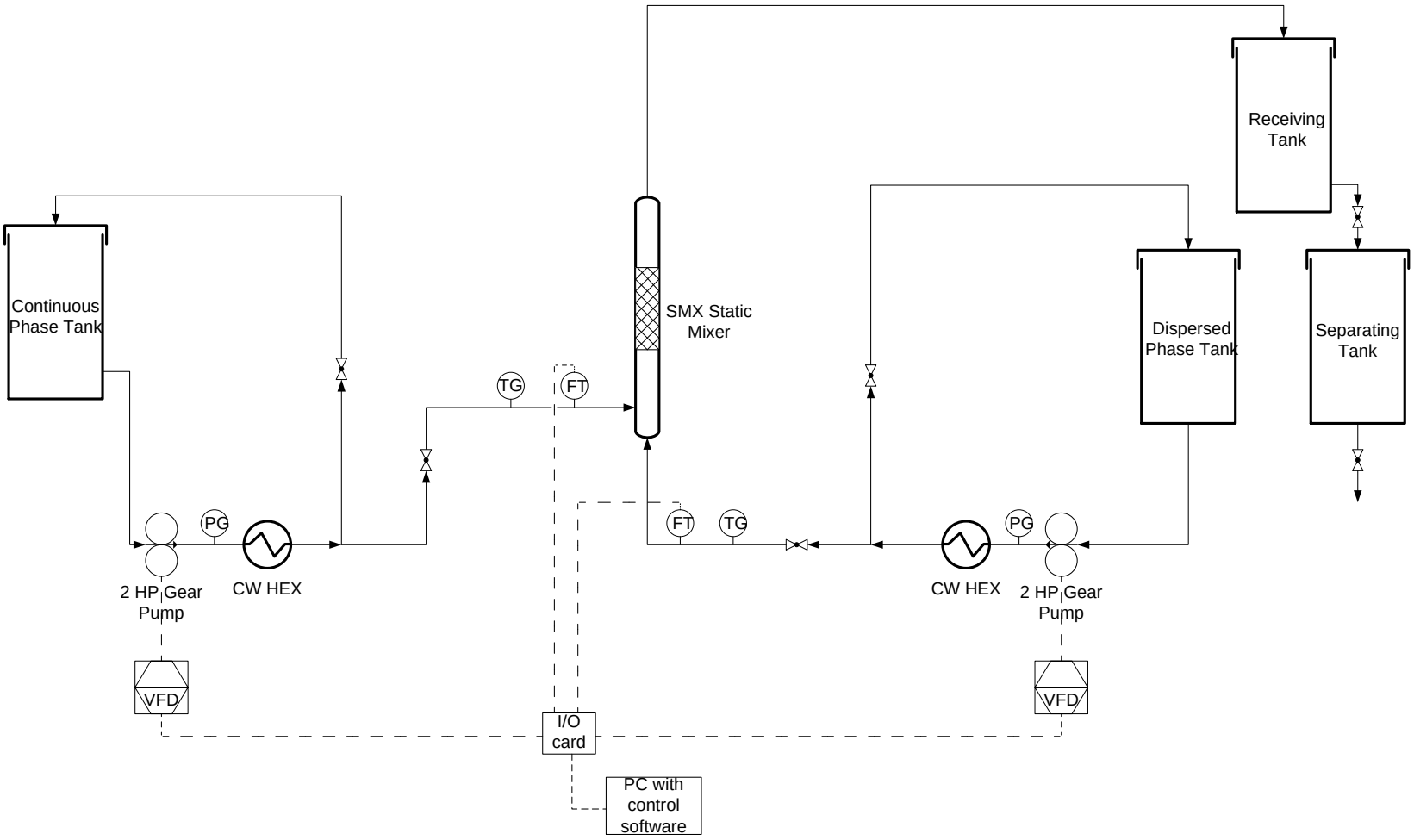

Figure 9. Process flow diagram with instrumentation

A 15 gallon (57 L) tank was used for the continuous phase to allow for enough run time to capture images at flow rates of up to 10 L/min. Flowserve rotary gear pumps (model no: 2GA) were used for both continuous and dispersed phase sides. These were run by 2 HP AC motors, which were controlled by a Variable Frequency Drive (VFD) that received frequency as an input from the PC. Omega positive displacement flowmeters (FPD1002B-A) were used to measure the volumetric flow rates. The flow rates were displayed on the monitor, and were manually controlled by changing the input frequency to the VFD, which ultimately changed the RPM of the motor. Recirculation lines were used to relieve system of backpressure, to homogenize the continuous phase after dilution and to clean the system. Heat exchangers were used only with high viscosity fluids and at high flow rates to maintain the operating temperature of 21^{o} C. For most runs they were on standby as the temperature on the thermometer did not show signs of temperature rise due to viscous dissipation. As shown in figure 10, two entry configurations were used for the static mixer. Continuous phase entered from the bottom centre of the mixer when it was at high viscosity (~200 mPaS) to allow the development for fully developed laminar flow. For the other two viscosity levels (70 and 25 mPaS), the continuous phase entered from the side through an L-shaped tube while the dispersed phase entered from the bottom.

In a typical run, the continuous phase pump would first be started and brought to a desired flow rate. The dispersed phase pump would then be started for a set flow rate that would achieve a desired holdup ϕ. The dispersion would then be captured by the flow visualization setup (described below). The liquids would separate in the separating tank, with the heavier cont. phase settling at the bottom. The continuous phase would then be drained and transported manually to the continuous phase tank for reuse. Since the silicone oil was bought in bulk and was the minor phase, it was seldom reused. Especially, for the low and high surfactant concentration levels, silicone oil was never used for more than one pass through the system. Surfactant build-up in the silicone oil phase was therefore avoided.

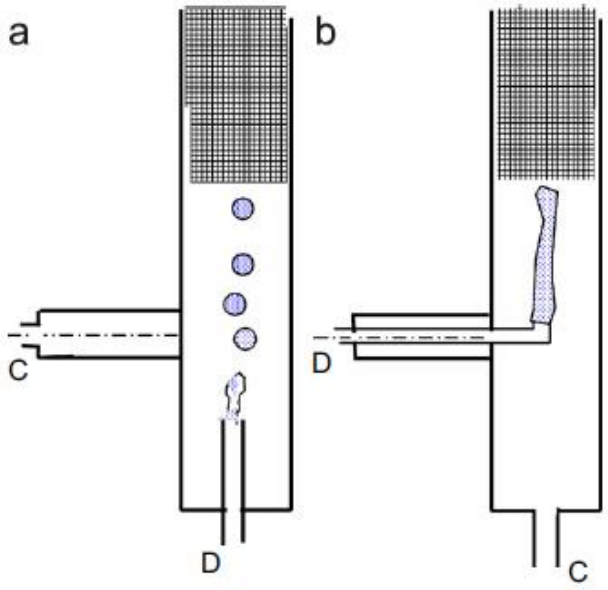

Figure 10. Entry configurations for continuous and dispersed phase:a) continuous phase (70 and 25 mPaS) entering from the side and dispersed phase entering from the bottom, b) continuous phase (200 mPaS) entering from the bottom and dispersed phase entering from the side (from Rao et al.,2007)

3.3 Flow visualization setup and image capture

Simple backlighting technique was selected for flow visualization (shown in figure 11). The light source was a 2000 lumens fluorescent white light bulb with a diffuser attached to the exterior of the mixer at the light end. At the other end, a Navitar 4X zoom lens was used with a Pixelfly QE camera, which is capable of capturing 1280x1024 images at 12 frames per second. The camera and the lens were placed on a manually controlled x-y-z positioner to precisely control the field of view and the focal plane. The plane closest to the wall was selected as the focal plane in order to minimize the possibility of out of focus droplets at the front of the plane obscuring the ones in it. The depth of field for the lens was determined to be 3 mm, and hence only the droplets within the first 3mm from the inner wall of the mixer were captured. The field of view was set about four inches from the top element.

For a typical run, a sample of 200 images was taken. This was determined to be sufficient as the number of droplets captured was enough for the mean and standard deviation to converge. The images were taken at a frequency such that the time period exceeded the time taken for a drop to pass through the field of view. PCO camware software was used to trigger the image capture and to handle the sequence of images. A 0.001 s exposure time was used for all images.

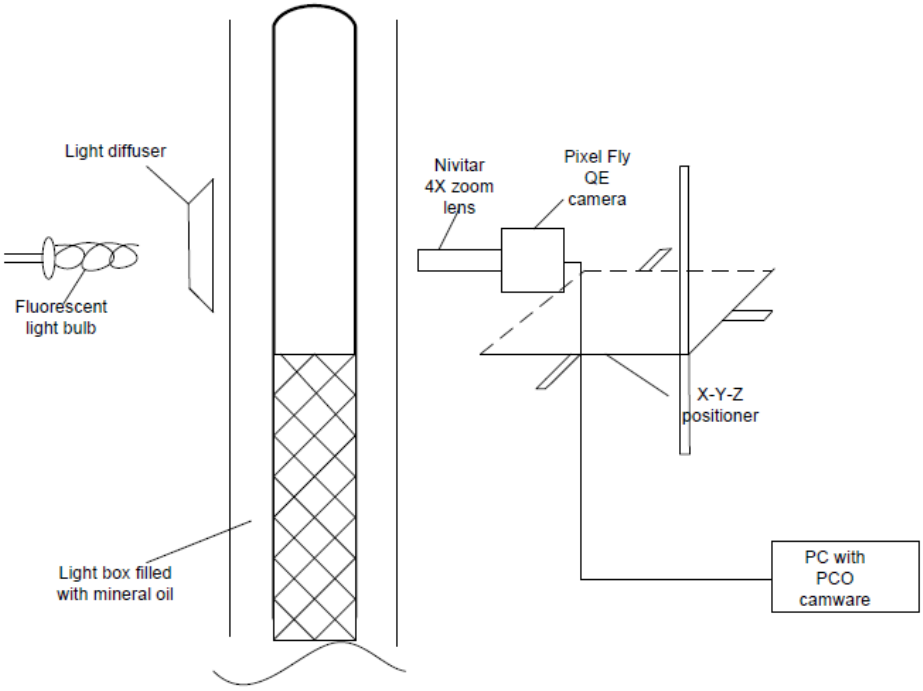

Figure 11. Flow Visualization Setup

3.4 Image processing and circle detection

The flowchart in figure 12 summarizes the code-in appendix B- that was used for image processing and circle detection. It was coded in C++ , with the OpenCV library of functions, which were used for each of the blocks in the flow chart. The functionality and the parameters of these functions are documented in Bradski & Kaehler (2008).

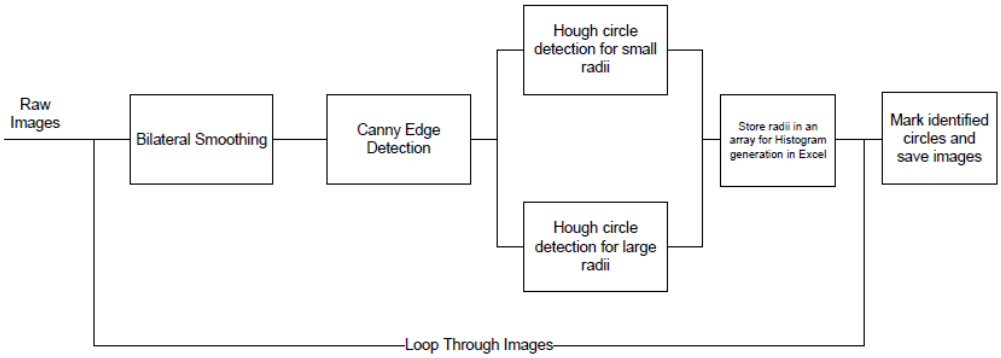

Figure 12. Flow chart for image processing code

In the pre-processsing steps an image first goes through bilateral smoothing. This is an edge preserving smoothing technique that is used to filter the high frequency noise in the image. It is akin to Gaussian smoothing, except in this case an additional parameter is used to specify the variance of the Gaussian filter in the colour domain. It then goes through Canny edge detection routine (described in Bradski & Kaehler (2008), pg. 151), where a gradient threshold is used as a parameter to ignore the edges that are less prominent. These edges would correspond to out of focus drops. The gradient threshold, therefore, is a key parameter that determines the tolerance to out of focus drops that lie outside the focal plane. Figures 13-15 illustrate the effect of these pre-processing steps for a sample raw image.

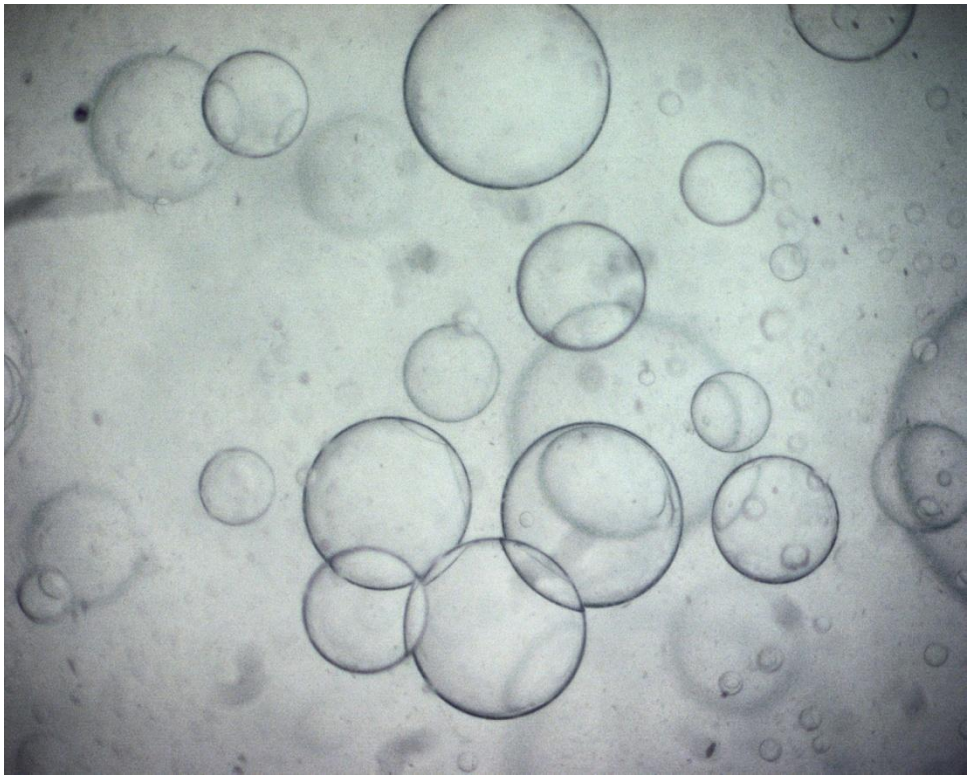

Figure 13. Sample raw image

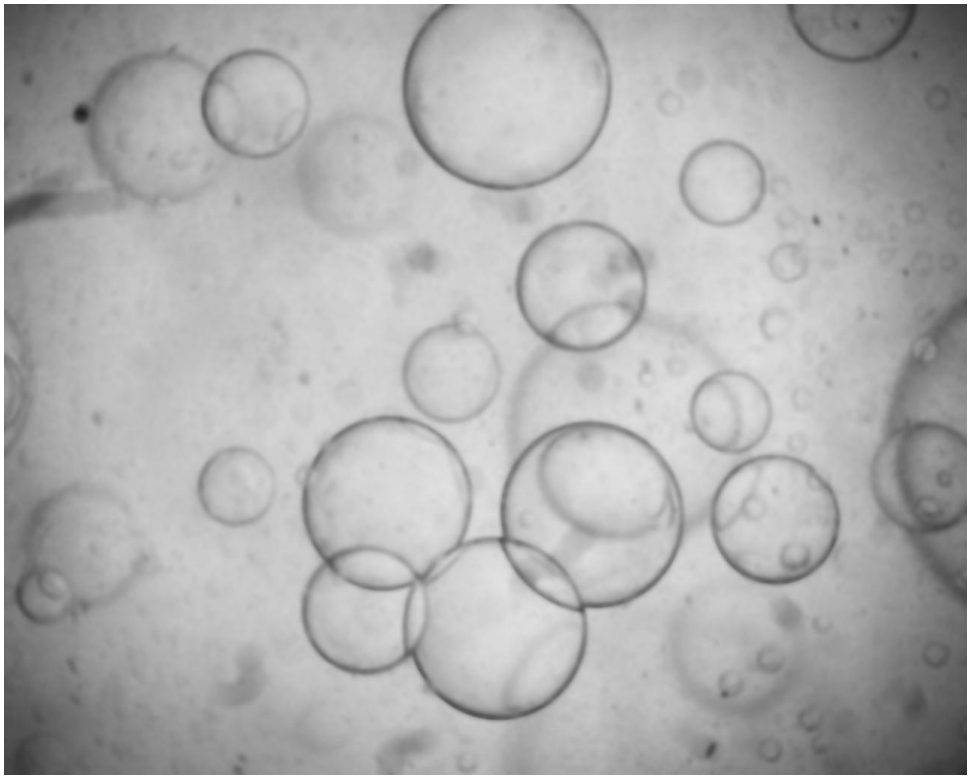

Figure 14. Effect of Bilateral Smoothing (edge preserving algorithm)-image is blurred except at the edges, which are still preserved

The binary image from the Canny edge detection routine is then used for the Hough circle algorithm that uses the 21-HT version (as described in literature review) of the algorithm. The source code for this function was slightly modified to improve the edge gradient direction calculated from Sobel derivatives. An important parameter in the Hough circle routine is the

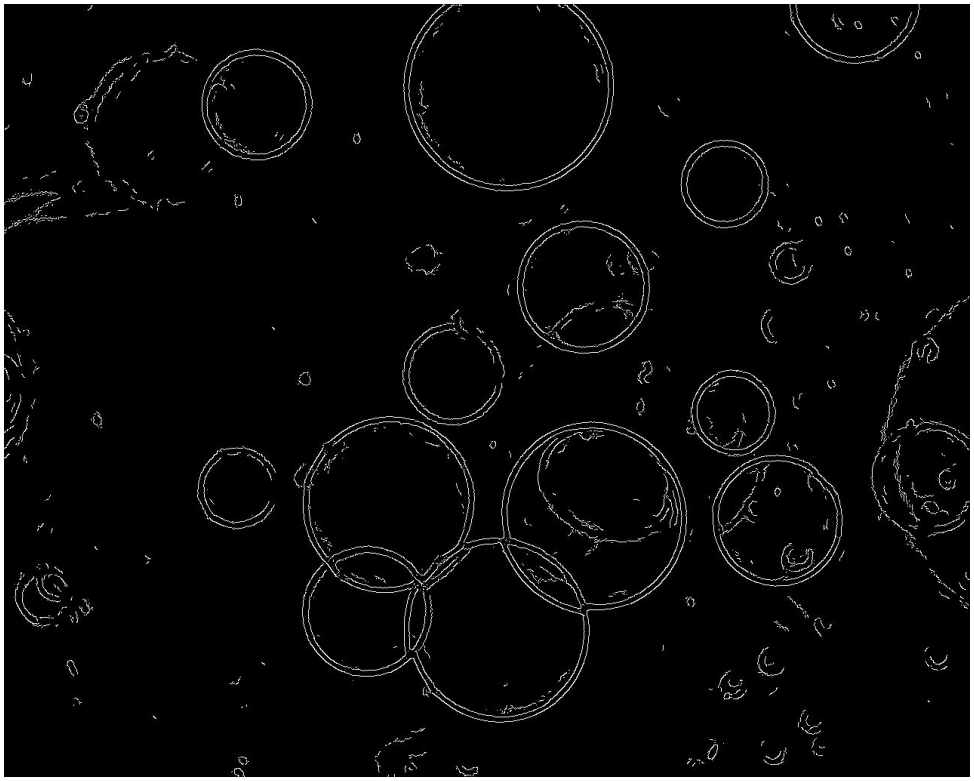

Figure 15. Binary image after Canny Edge detection

accumulator threshold, which determines the minimum number of votes that is required in order to be included in the local maxima detection in the 2D-array. Since the number of votes is directly proportional to the radius of the circle, the function has to be called multiple times depending on the range of radii. This is because for large radii range, the accumulator threshold either becomes too low for large radii, or too high for small radii, which in turn respectively increases the propensity of exclusion of smaller droplets or false detection of large droplets. In this case, the function was called upon separately each for two groups of radii, and the optimum threshold was determined on a trial an error basis. Figure 16

shows the circles detected by the Hough circle routine for the sample raw image. The recall and precision for this sample image are both 100%.

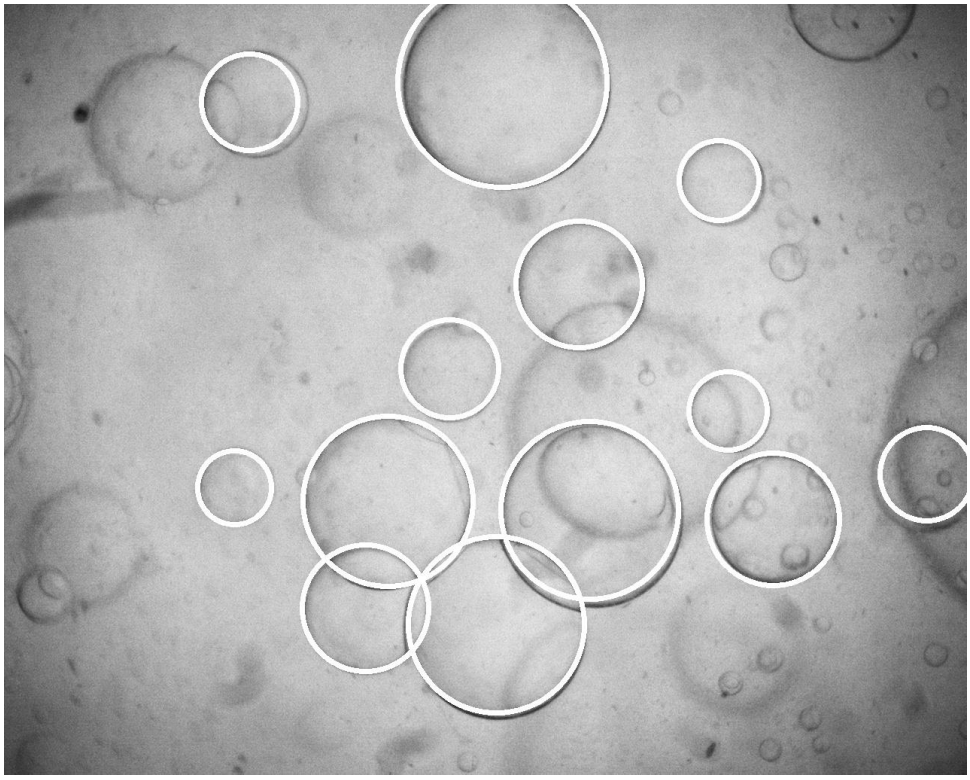

Figure 16. Identified Droplets

There are a few salient points on the overall performance of the algorithm that were seen during the entire course of experimentation. They are as follows-

-Droplets less than 40 pixels in diameter were difficult to detect. This is because the edges for small droplets (especially at high magnification) were not prominent. Furthermore, the accumulator threshold for the group of small radii, was set higher for radii < 20 pixels to qualify for local maxima detection

- The performance of the algorithm is sensitive to the quality of the images. At high flow rates, the images taken were affected by motion blur and were not as sharp as the sample image shown above. In these cases, the algorithm had higher rates of false positives for radii ranging between 80-90 pixels. This affected the distribution by introducing false peaks, and also affected D_{43} by adding a small negative bias.

-The key parameters such as Canny edge threshold and the accumulator threshold parameters had to be fine tuned for different image qualities. The algorithm therefore cannot be considered as a plug and play function that would work in all scenarios.

3.5 Note on measurement errors

Table 3 gives the relative errors of measured and calculated values. Except for mass, volume and viscosity, the relative errors of other directly measured quantities are based on observation.

Table 3. Relative errors of measured and calculated values

Quantity	Relative error
volume, V	±5%
mass, m	±1%
density, ρ	±6%
interfacial tension, σ	±10%
viscosity, μ	±1%
flow rate, Q	±5%
superficial velocity, u	±5%
capillary number, Ca	±16%
reynolds number, Re	±12%

Error estimate on D_{43} measurement can only be obtained by comparing the true value to the measured values for a large number of data points. Because a true value can only be obtained by manually measuring the drops, such an exercise is infeasible given the scope of the research. We can however, identify the sources of random and systematic errors. Sources of systematic errors are-sampling near the wall of the mixer, limited resolution of the algorithm to detect small droplets and the algorithm`s sensitivity to image quality-which can cause a negative bias from false positives for poor quality images. Random errors can be attributed to drops passing behind and in front of the focal plane, which can cause changes in light intensity and visibility of drops in the focal plane. These errors should be small when compared to the systematic errors. Furthermore, because the algorithm process ~200 images (~1000 droplets) to obtain a single D_{43} measurement, we obtain less variability in measurement, and hence we can say that the algorithm is not significant source of random error.

4. Results and Discussion

Appendix A contains the experimental data in tabulated form. The data were mainly collected using the 41.18 mm diameter mixer. It was originally planned to collect similar data with a smaller 15.75 mm diameter mixer, however due to time constraints only a very limited number of runs was obtained.

It is to be noted that the effect of holdup (dispersed phase fraction) was studied only for the case of no added surfactant, and only with continuous phase viscosities of 25 and 70 mPa.S, and at certain flow rates. Since the effect was minor, these points appear as clusters in the figures that follow. The rest of the data sets were obtained at a constant holdup of 10%, while varying the superficial velocity.

4.1 D_{43} trends

The D_{43} measure has been used instead of the Sauter mean diameter (D_{32}) because it places more emphasis on the larger size droplets and is therefore better in this case as distributions from SMX mixers exhibit a significant tail. Moreover, it is less sensitive to exclusion of smaller diameter droplets, and hence is even more appropriate with the measurement system used, which has a limited recall for smaller diameters.

Figures 17, 18 and 19 show the effect of interfacial tension on D_{43} for continuous phase viscosities of 25, 70 and 200 mPaS respectively. The values of D_{43} have been plotted against superficial velocity to simultaneously demonstrate the effect of interfacial tension. Low (~200 ppm) and high (~1000 ppm) surfactant concentrations correspond to interfacial tensions of 20 and 12 mN/m respectively, and are represented by slashes and crosses on the markers respectively.

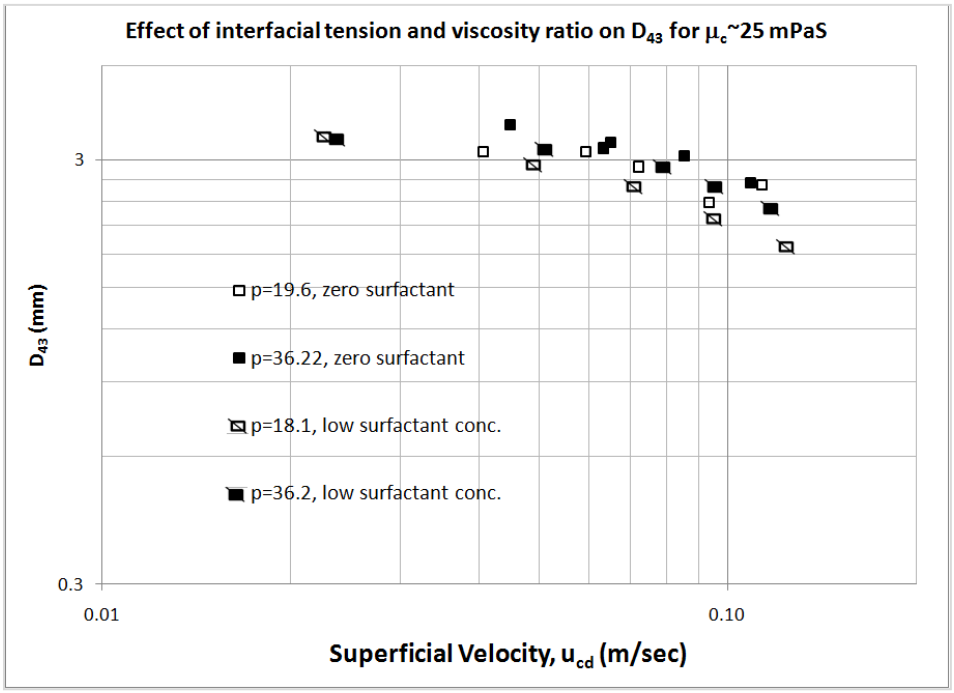

Figure 17. Log-log plot to show the effect of interfacial tension and viscosity ratio on D_{43} for μ_c ~25 mPaS (low and high surfactant conc. correspond to 200 and 1000 ppm respectively)

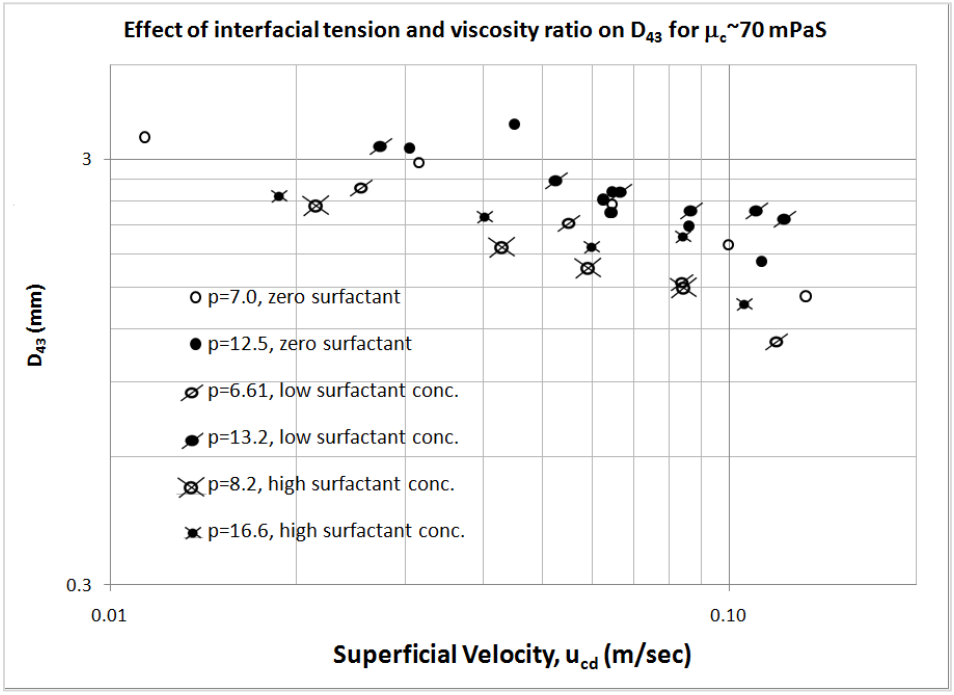

Figure 18. Log-log plot to show the effect of interfacial tension and viscosity ratio on D_{43} for μ_c ~70mPaS

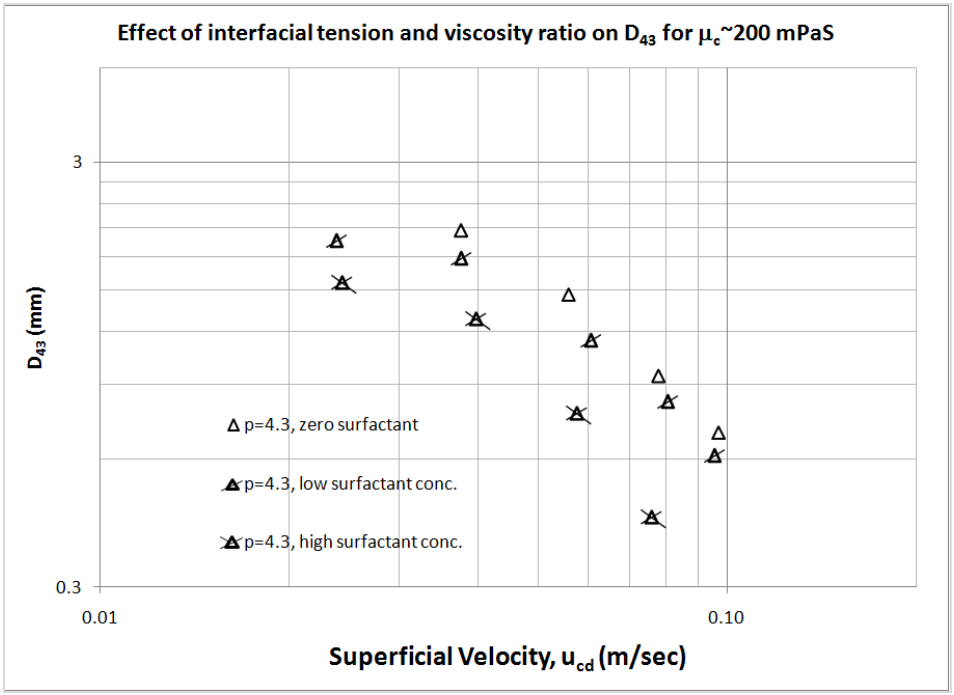

Figure 19. Log-log plot to show the effect of interfacial tension and viscosity ratio on D_{43} for μ_c ~200 mPaS

From the plots above, it can be seen that D_{43} decreases by lowering the interfacial tension. However, the effect is less apparent at low surfactant concentration. It is known that surfactants have diffusion kinetics (Zhang et al., 1999), and one can speculate that this discrepancy could arise because the interfacial concentration at a moving surface is less than the equilibrium value, which would result in interfacial tension being larger than the measured value. Furthermore, it can be seen in Fig. 17 &18 that except for the zero surfactant case, the D_{43}s are higher for the high dispersed phase viscosity (1000 cst. oil) for a specific paring with continuous phase viscosity. These observations, combined with the clear effect of the superficial velocity, suggest that the drop breakup is a function of the capillary number ($Ca=\mu_c u_{cd}/\sigma$) and the drop viscosity, which is conventionally taken into account with the viscosity ratio.

Figures 20, 21 and 22 show the effect of viscosity ratio on D_{43} at different surfactant concentration levels. The data is the same for the plots above, except that they have been regrouped to illustrate the effects of viscosity ratio.

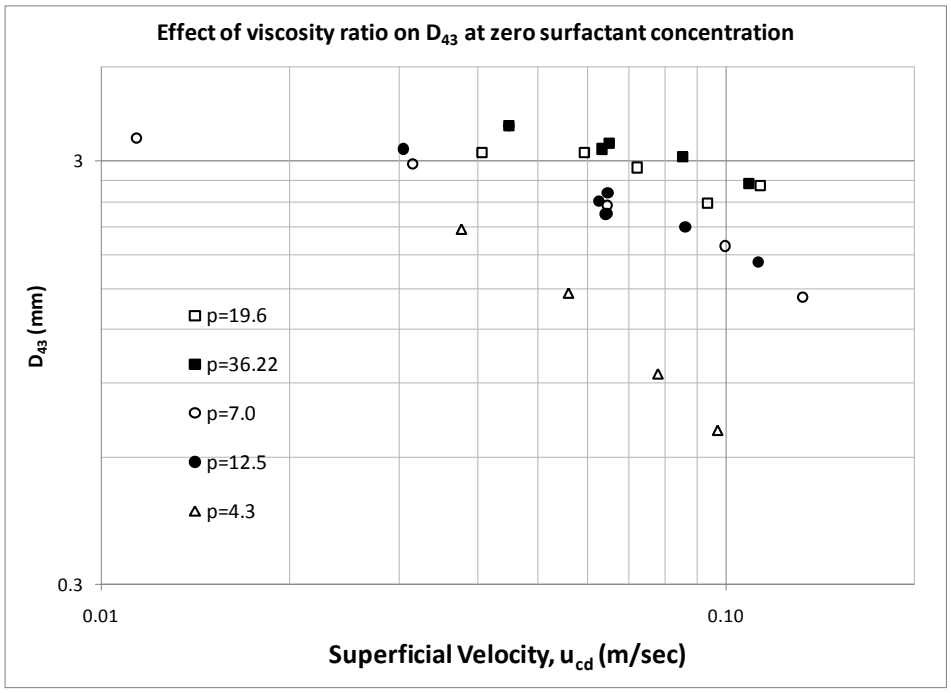

Figure 20. Log-log plot to show the effect of viscosity ratio on D_{43} at zero surfactant concentration (viscosity ratios arranged with respect to continuous phase viscosities- from 25 mPaS (squares) to 200 mPaS (triangle); black fill represents pairing with 1000 Cst. oil whereas no fill represents pairing with 500 Cst. oil)

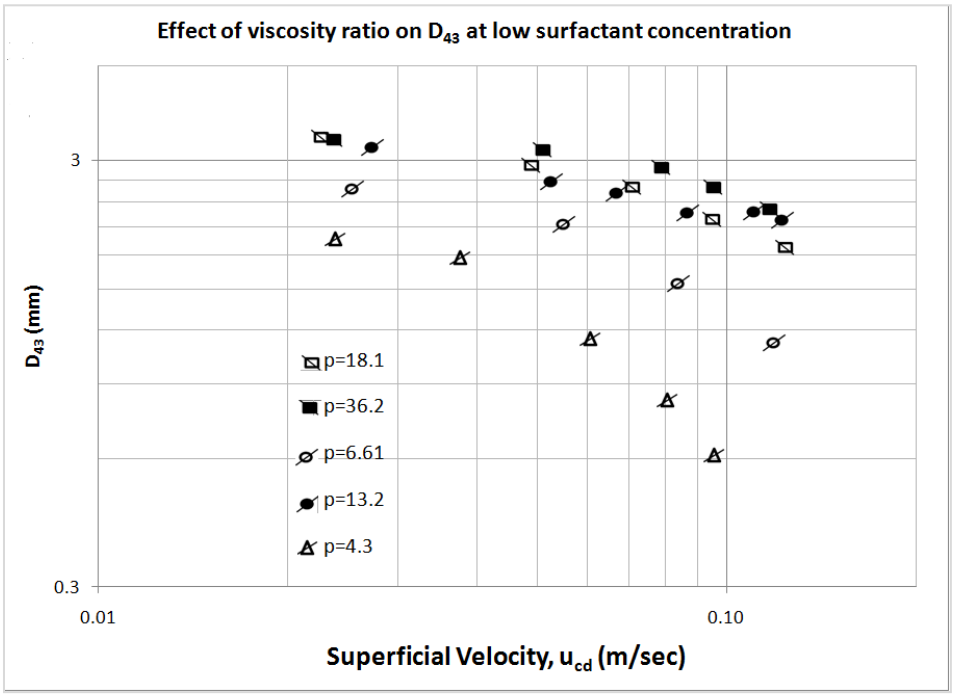

Figure 21. Log-log plot to show the effect of viscosity ratio on D_{43} at low surfactant concentration

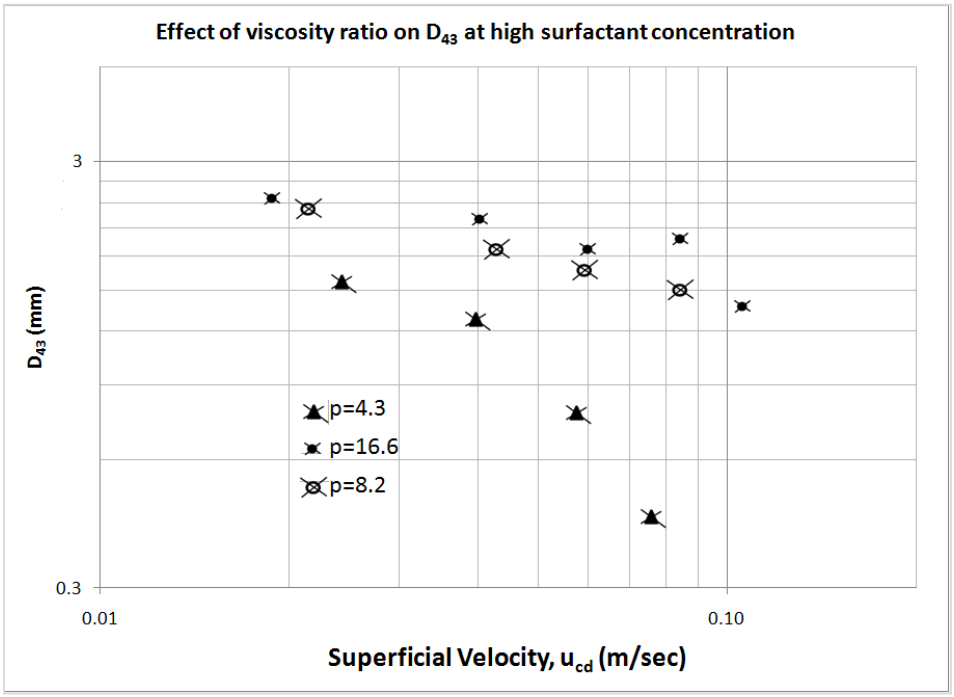

Figure 22. Log-log plot to show the effect of viscosity ratio on D_{43} at high surfactant concentration

From Figures 20-22, we see that D_{43} has a stronger correlation with the continuous phase viscosity- more so than the viscosity ratio. The trend is very consistent across all surfactant concentration levels, in that we see that D_{43} decreases with increasing continuous phase viscosity. However, for a specific continuous phase viscosity, D_{43}s are higher when paired with the 1000 cst. oil than paired with the 500 cst. oil. Again the results indicate that hydrodynamic and surface forces are at play here.

Figure 23 shows the effect of the number of elements on D_{43}. The numbers were varied between six and ten.

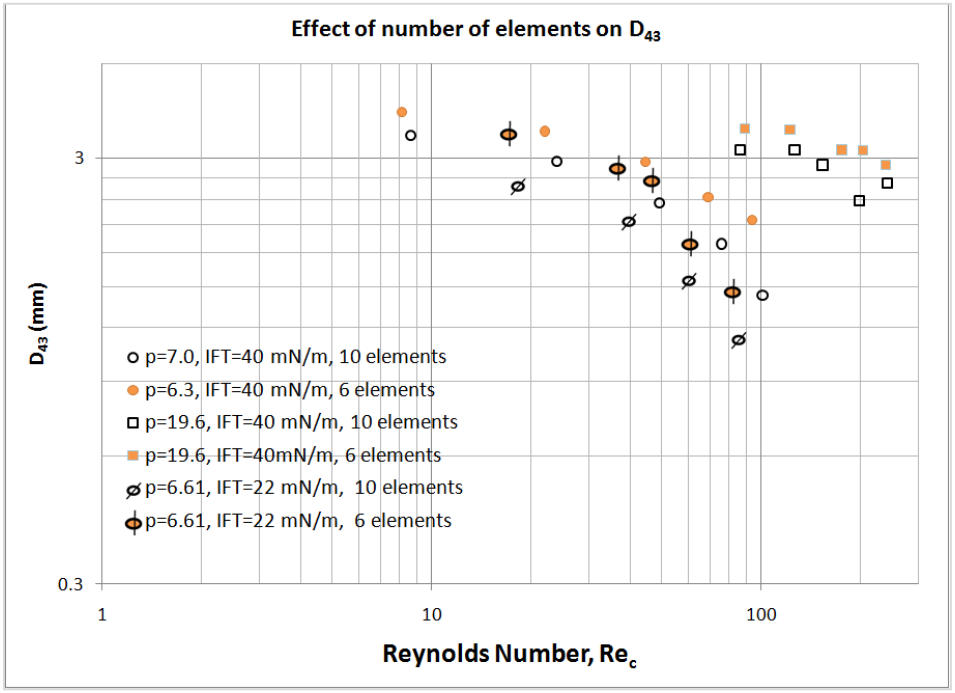

Figure 23. Effect of number of elements on D_{43}

The values of D_{43} are consistently higher with six elements. Since the system is dilute ($\phi \sim 10\%$), this observation cannot be attributed to drop coalescence. As mentioned in Fradette et al. (2007), in addition to the nature of the flow field, the residence time inside the mixer elements is very important. If the mean residence time is less than the time required to break the drop then size reduction may not be achieved. This phenomenon can also be modelled by the equation given by Middleman (1974).

4.2 D_{max} trends

Figures 24, 25 and 26 show the effect of Interfacial tension and superficial velocity on D_{max}, which is the maximum droplet size found in the distribution.

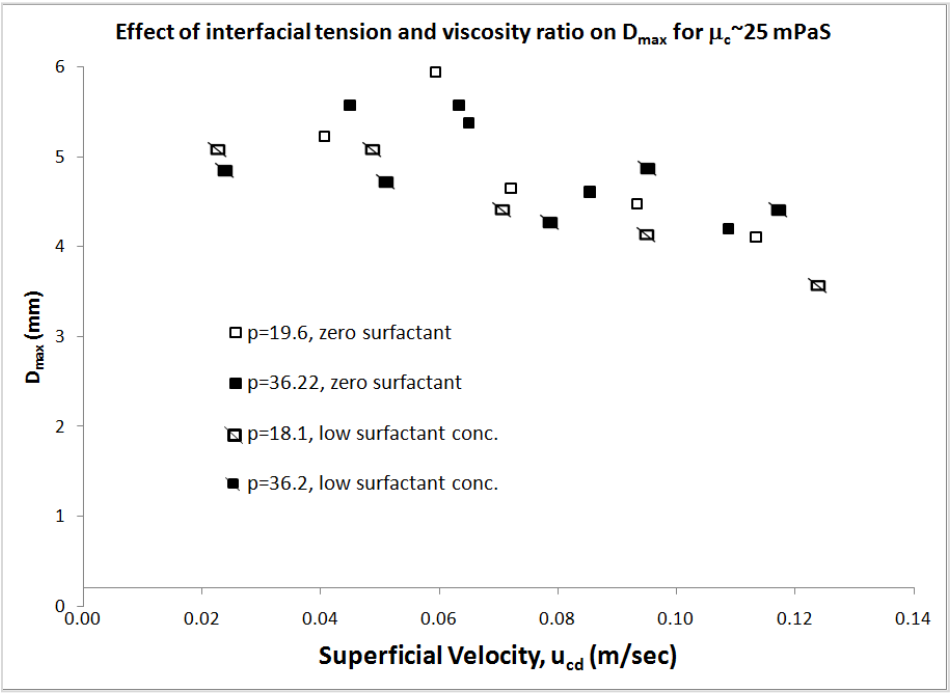

Figure 24. Effect of interfacial tension and viscosity ratio on D_{max} for μ_c ~25 mPaS

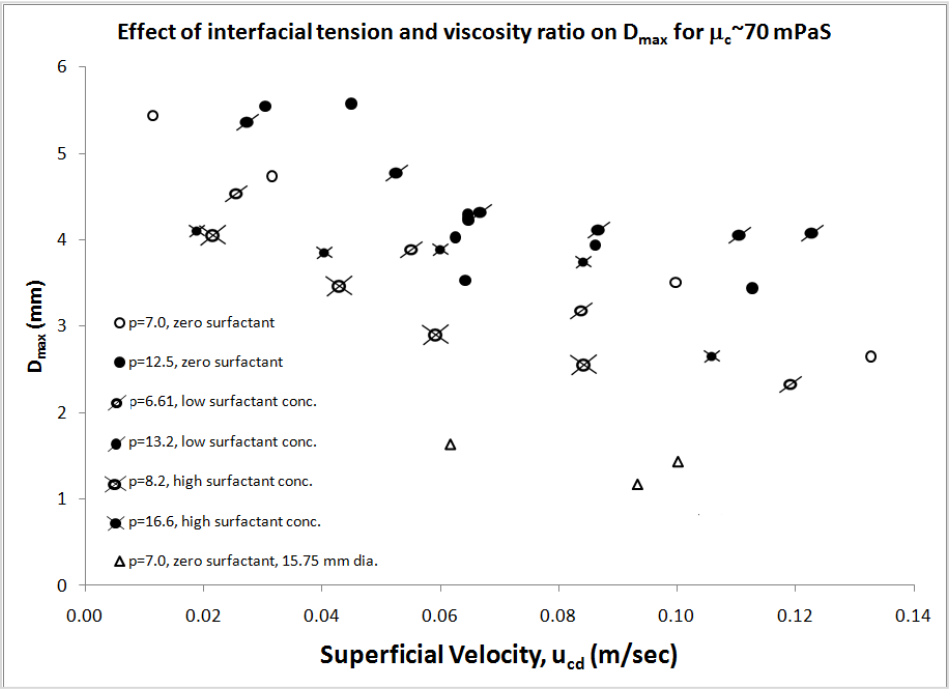

Figure 25. Effect of interfacial tension and viscosity ratio on D_{max} for μ_c ~70 mPaS

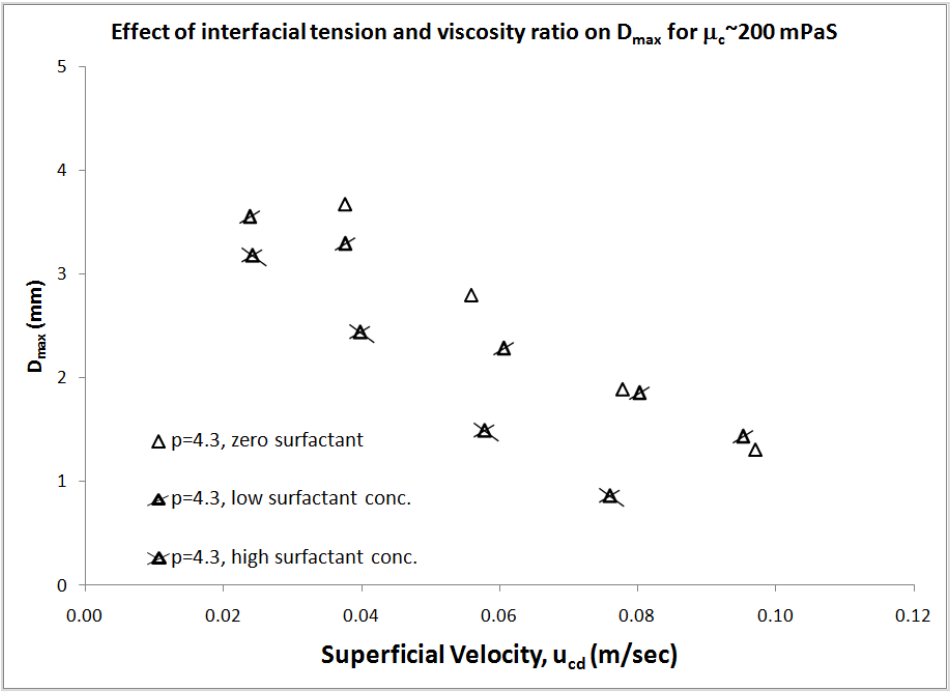

Figure 26. Effect of interfacial tension and viscosity ratio on D_{max} for μ_c ~200 mPaS

It can be seen that for low continuous phase viscosity and zero surfactant concentration, Dmax is in the vicinity of 5 mm. Very limited data was also obtained with a mixer diameter of 15.75 mm. Dmax values for these three runs were approximately ~1.5 mm. These two values are very close to the measured gaps (5 mm and 1.5 mm respectively) between the cross bars for 41.18 and 15.75 mm diameter mixer elements. This observation suggests that there is effectively a slicing action of the crossbars to determine the initial drop size. If these drops are not broken any further, due to inadequate hydrodynamic forces or residence times further up the mixer, then they appear as oversize drops in the distribution. This "slicing" action is also shown in the section *Qualitative Images* below.

4.3 Droplet size distribution trends

Table 4 compares the droplet size distributions at low and high superficial velocities and at different viscosity ratios-all obtained at zero surfactant concentration. The low values range from 1.5-2 L/min, whereas the high values range from 6-8 L/min (Please see Appendix A for specific values for the given run numbers).

Table 4. Droplet size distribution trends at zero surfactant concentration

	Superficial Velocity	
	Low	***High***
p=36.2 (μ_c=27 mPaS, μ_d=978 mPaS)	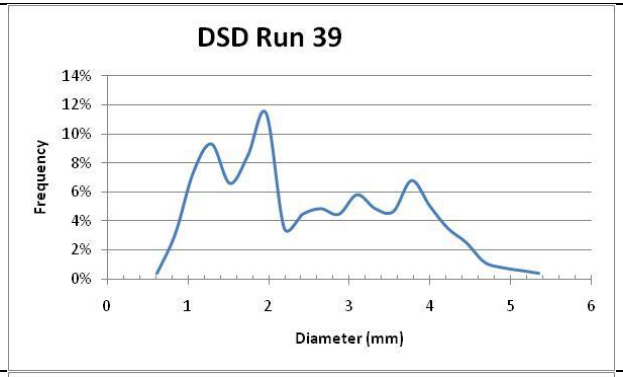	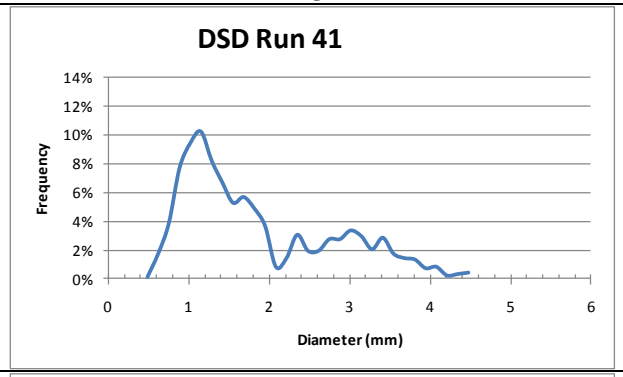
p=19.6 (μ_c=27 mPaS, μ_d=489 mPaS)	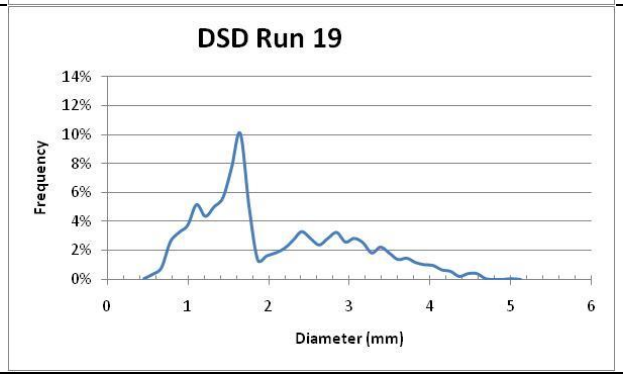	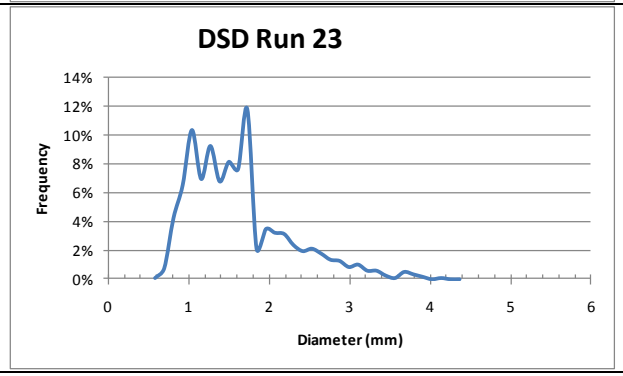

	Superficial Velocity	
	Low	***High***
p=12.5 (μ_c=78 mPaS, μ_d=978 mPaS)	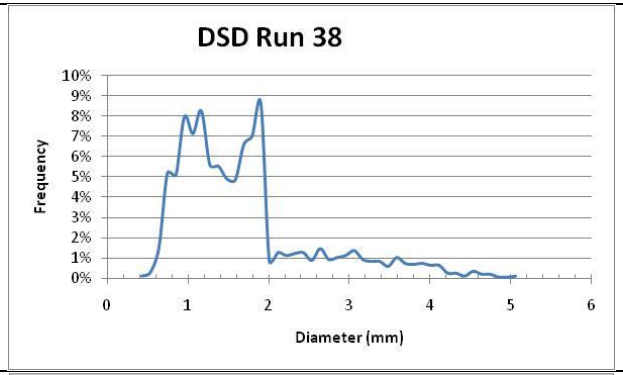	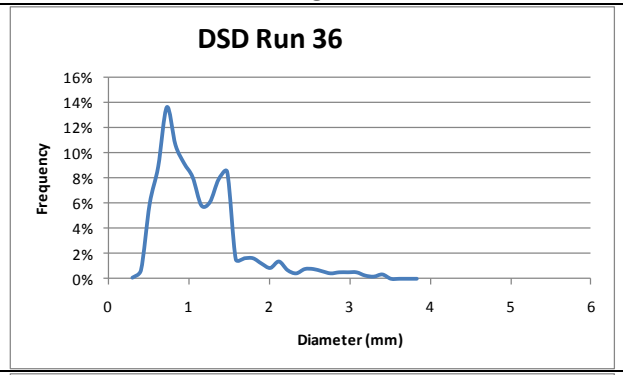
p=4.3 (μ_c=230 mPaS, μ_d=489 mPaS)	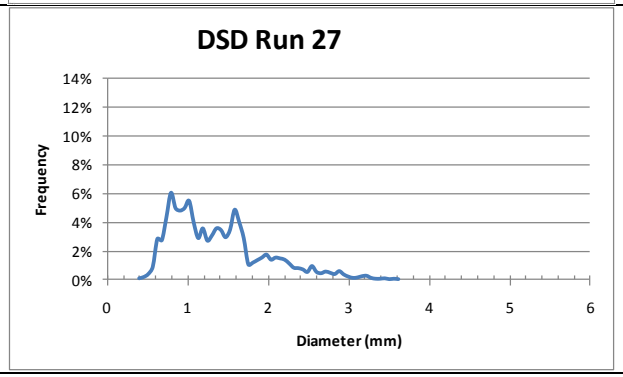	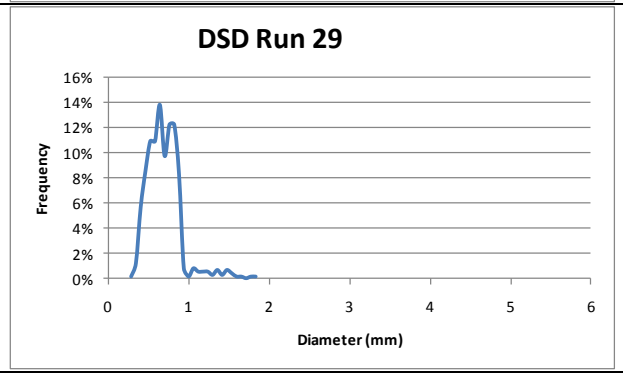

The general trend for these distributions is that the frequency of occurrence is more or less the same (i.e. we see a plateau) in a specific diameter range. This is followed by a tail that becomes smaller and narrower with increasing continuous phase viscosity and superficial velocity. As explained in the previous section, it can be inferred that for a given residence time inside the mixer, size reduction is achieved as the hydrodynamic forces increase in relation to the interfacial forces. For some runs-as in Run 38 for example-the distributions show a sharp cutoff in the droplet size. This however, is a result of the Hough circle detection algorithm's propensity to detect false positives within a range (which in this case is 2 mm) when the image quality is poor.

Table 5 compares the same, but at high surfactant concentration (~1000 ppm).

Table 5. Droplet Size Distribution Trends at High Surfactant Concentration

	Superficial Velocity	
	Low	***High***
p=16.3 (μ_c=60 mPaS, μ_d=978 mPaS)	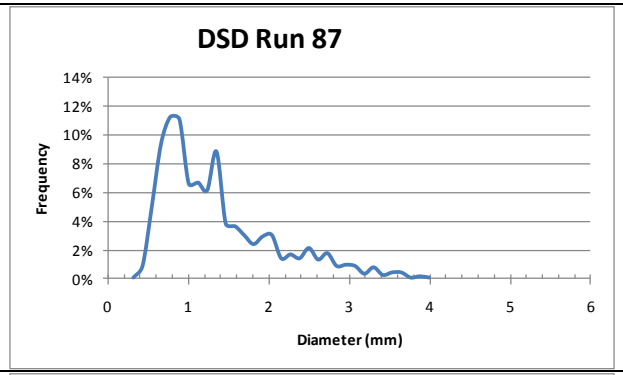	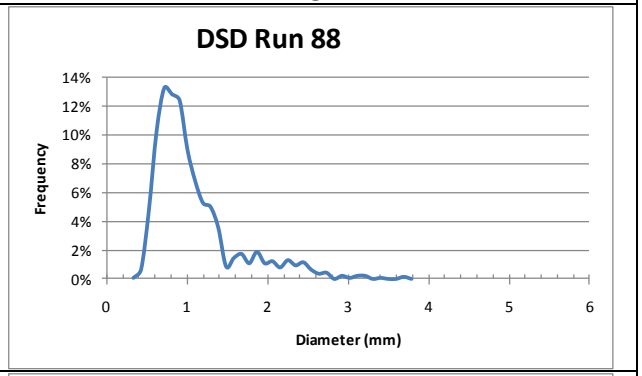
p=8.2 (μ_c=60 mPaS, μ_d=489 mPaS)	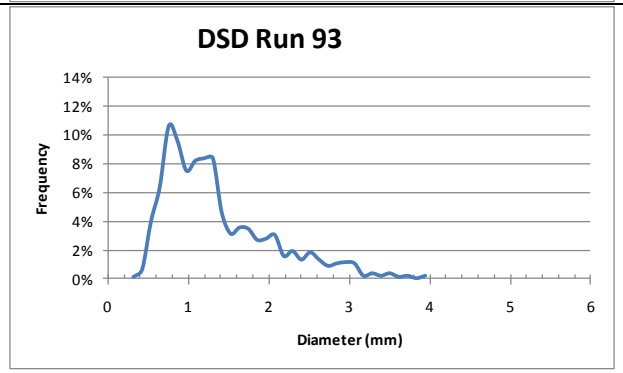	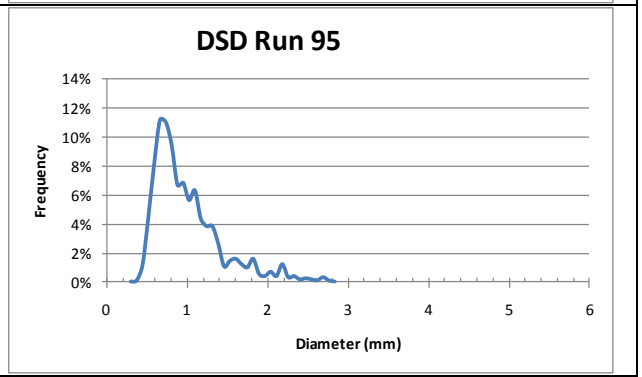

	Superficial Velocity	
	Low	***High***
p=4.3 (μ_c=230 mPaS, μ_d=978 mPaS)	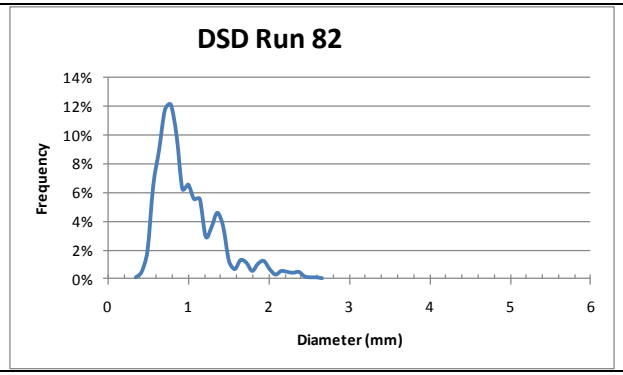	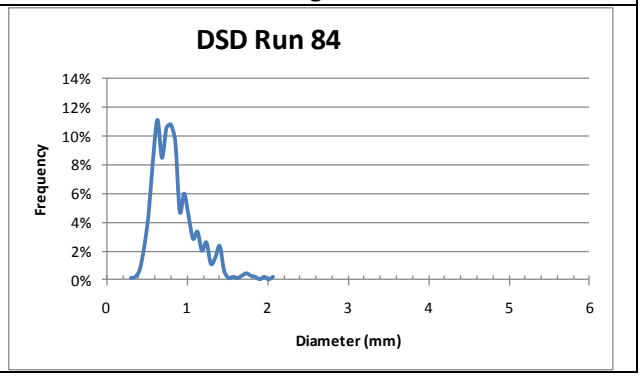

We see that at high surfactant concentration the distributions tend to resemble a log-normal distribution. It tends towards becoming a Gaussian (as in the case with run 84), with increasing superficial velocity and continuous phase viscosity. This could be because of a change in breakup mechanism as a result of the addition of surfactant. A possible candidate for a dominant mechanism could be tip streaming, since the breakup of a large number of daughter droplets from the tip of a large mother droplet gives rise to a log-normal distribution. This conjecture is further supported by Janssen (1997), wherein tip streaming has been described as being more favourable with moderate surfactant concentration.

4.4 Qualitative Images

Images were also taken inside the third element (from the bottom) of the mixer. The purpose of this was to get a qualitative view of the drop breakup mechanism inside the mixer. Figure 27 shows the breakup of a stream as it passes through the gap between the crossbars. In figure 28, an image sequence is shown that demonstrates the drop breakup from collision with cross -points as described in Liu (2005) and shown in Figure 29.

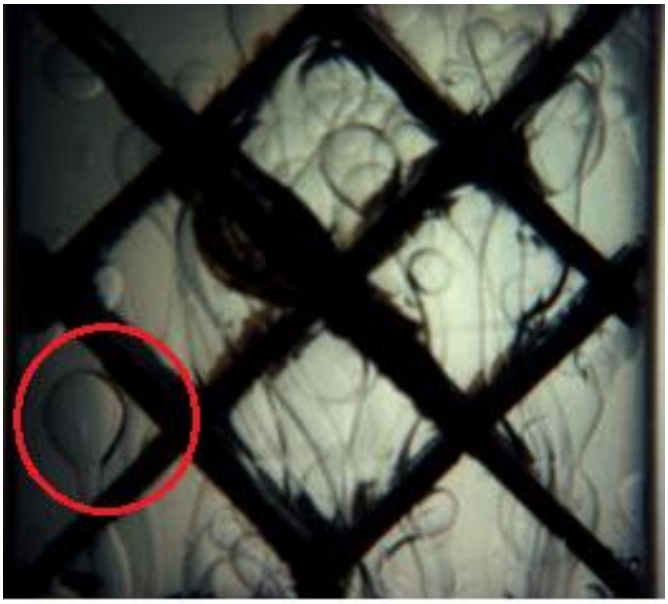

Figure 27. A frame from an image sequence showing the breakup of a dispersed phase stream into drops as it is passes through the gap between the cross bars

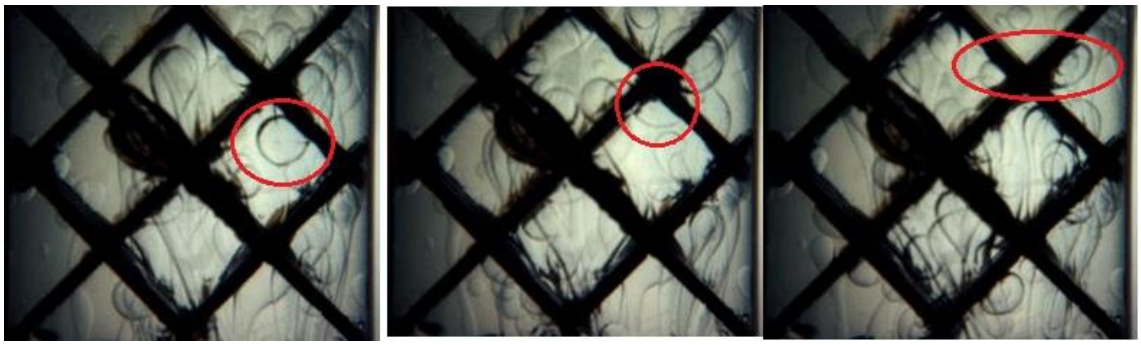

Figure 28. Image sequence showing drop breakup from impact with cross-points of the packing

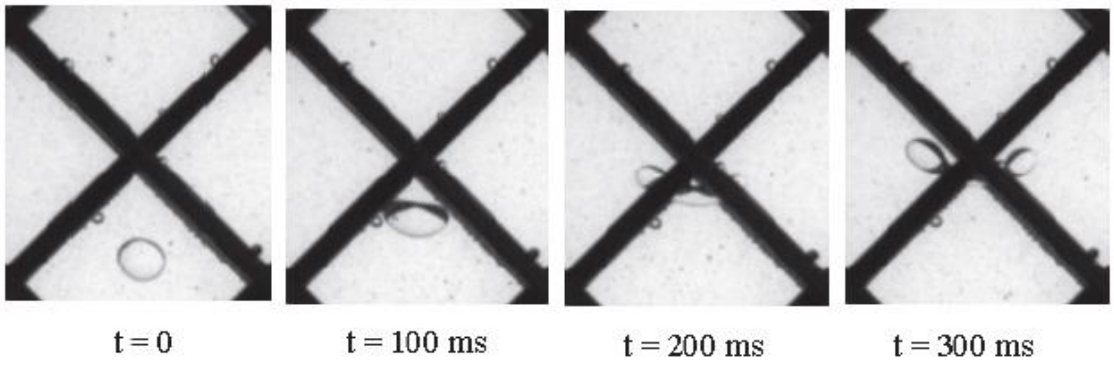

Figure 29. Image sequence showing a single drop breakup at cross-point (Liu, 2005)

From the images above, we can conclude that there are multiple breakup mechanisms occurring inside the mixer. Furthermore, as seen in fig. 27, the slicing mechanism is seen wherein the dispersed phase stream is stretched as it passes through the gap between the cross bars, and ultimately breaks due the extensional and compression regions in the surrounding three dimensional flow field.

4.5 Proposed Model

An observation-based model has been proposed by Dr. Baird. A drop can be said to breakup in a 2-stage process-

-The first stage is the initial formation of primary drops (with diameter D_0), which forms with the interaction with the packing. The diameter D_0 is of the same order of magnitude as the gap between the adjacent plates in the packing.

-Secondary drops with diameter, $D<D_0$ are formed by a mechanism of viscous shear as described in Janssen et al. (1997) and Christini et al. (2003). The final distribution contains a few relatively large drops and a much larger number of smaller ones.

We equate the work done by viscous shear with the increase in surface energy owing to the size reduction from D_0->D_f. Consider a large number of N_0 drops of diameter D_0 undergoing breakup to diameter D_f ($<D_0$). Then by continunity the number of drops N is given by

$$N = N_0 \left(\frac{D_0}{D_f}\right)^3 \tag{28}$$

and the relative increase in surface area is given by

$$Increase\ in\ surface\ area = N\pi {D_f}^2 - N_0\pi {D_0}^2 \tag{29}$$

from eq (28) and (29), the above simplifies to

$$Increase\ in\ surface\ area = N_0\pi {D_0}^2 \left[\left(\frac{D_0}{D_f}\right) - 1\right] \tag{30}$$

Therefore the increase in suface energy per single drop is given by

$$Increase\ in\ surface\ energy = \pi {D_0}^2 \left[\left(\frac{D_0}{D_f}\right) - 1\right]\sigma \tag{31}$$

where σ is the interfacial tension.

Work done on the initial drop by viscous shear is proportional to

$$Work \propto viscous\ shear\ stress * surface\ area * length\ dimension \tag{32}$$

By assuming a shear rate of $\left(\frac{u}{D_0}\right)$, the proportionality above can be written as

$$Work \propto \mu_c \left(\frac{u}{D_0}\right) * {D_0}^2 * D_0 = \mu_c u_{cd} {D_0}^2 \tag{33}$$

Since the increase in surface energy is proportional to work done for breakup we get,

$$\pi {D_0}^2 \left[\left(\frac{D_0}{D_f}\right) - 1\right] \sigma \propto \mu_c u_{cd} {D_0}^2 \tag{34}$$

which simplifies to

$$\left(\frac{D_0}{D_f}\right) - 1 \propto \frac{\mu_c u_{cd}}{\sigma} = Ca \tag{35}$$

where Ca is the capillary number. Therefore D_0, D_f and Ca can be related by the equation

$$\left(\frac{D_0}{D_f}\right) - 1 = kCa \tag{36}$$

where k is an unknown proportionality constant. However, we now have a basis to plot the data. If we assume $D_f \approx D_{43}$, then we can plot $1/D_{43}$ Vs Ca, where the intercept would be $1/D_0$.

In Figure 29, $1/D_{43}$ has been plotted against $Ca * p^n$ where p is the viscosity ratio . Since the dispersed phase viscosity has not been considered in the above energy analysis, the capillary number has been multiplied by the viscosity ratio to the nth power. The value of the exponent n that gives the best linear fit has to be determined. Furthermore, since we suspect that the actual interfacial tension is higher than the measured interfacial tension because of diffusion kinetics, a reduction factor is used. It is the fraction of reduction of the

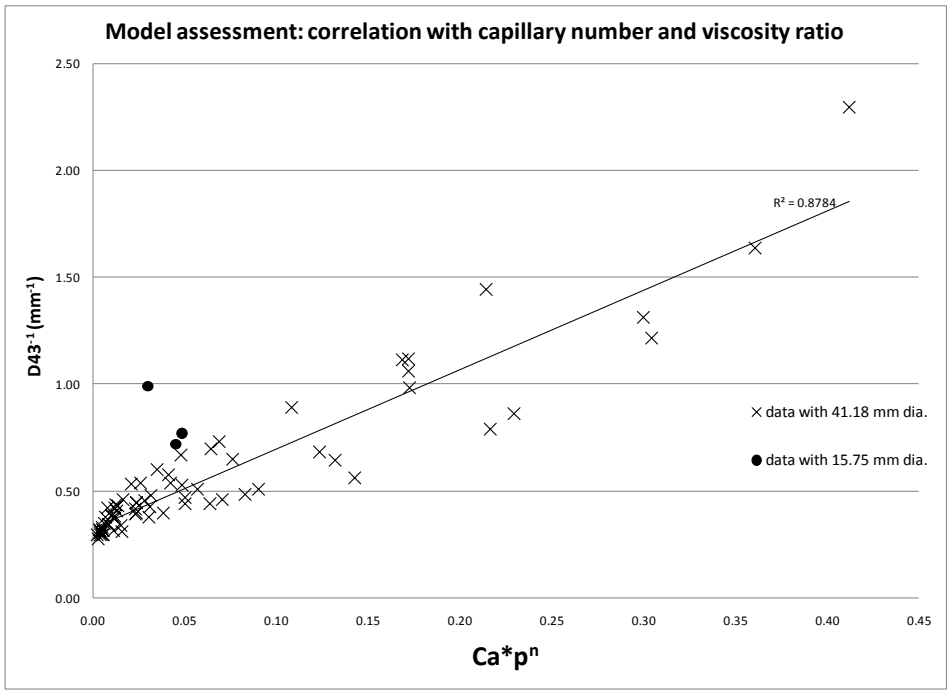

Figure 30. Model assessment by correlating D_{43} with capillary number

interfacial tension from zero surfactant to low or high surfactant concentration. From Excel solver, the best values of n and the reduction factor were determined to be -0.66 and 0.98 respectively. This gives a reasonably good fit with a R^2 value of 0.88. The trend line (for 41.18 mm dia.) intercepts the vertical axis at approximately 0.25, which corresponds to D_{43} ≈4 mm. Although, the data set for the 15.75 mm dia. is not large enough to substantiate any claim, however, it does seem to intercept the y-axis at ~0.6 mm, which corresponds to a D_{43}≈ 1.7 mm. Since both 4 mm and 1.7 mm are values that we might expect for D_0, we can say that the model is a good starting point. It might be improved by considering the effect of internal resistance of the drop phase viscosity in the energy analysis.

5. Conclusion

5.1 Summary

In this research, liquid-liquid dispersion of viscous fluids was studied in an SMX static mixer in the laminar regime. Backlighting technique was used for flow visualization, and Hough transform for circle detection was used in OpenCV to automatically detect and measure drops for obtaining the size distribution. Silicone oil and an aqueous solution of high fructose corn syrup were used for dispersed and continuous phases respectively, and sodium dodecyl sulfate was used as the surfactant to lower the interfacial tension. Experiments were conducted at varying viscosity ratios and flow rates-each at zero, low and high surfactant concentrations. The effect of holdup was explored only at specific viscosity ratios and at certain flow rates, and it was found to have a minimal effect on D_{43}. Further observations made were the following-

- Superficial velocity and continuous phase viscosity seemed to have a dominant effect on D_{43}. The effect of dispersed phase viscosity was significant only at low and high surfactant concentrations.
- There was a measurable decrease in D_{43} at low surfactant concentration, and a significant decrease at high surfactant concentration. This confirmed that there is an effect of interfacial tension.

- Droplet size distributions typically were found to have a long and wide tail, which became narrower and shorter with higher superficial velocities, higher continuous phase viscosities, and lower interfacial tension. For the lowest interfacial tension (high surfactant concentration), the size distribution was log-normal.
- The gap between cross bars (or adjacent plates) in the packing seemed to determine a primary diameter, which appeared as Dmax in the absence of major dispersion further up in the packing. This observation is consistent with Catalfamo et al. (2003), whereby size reduction during scale up was maintained by keeping the surface area to void volume ratio of the elements constant. This was done by addition of more cross bars for larger diameter elements.

Finally, a simple model relating D_{43} to capillary number was proposed (by Dr. Baird). The model is based on equating the work done in breaking a primary drop by hydrodynamic forces to the increase in surface energy of the drops. It was found to fit the data reasonably well, and it could prove to be a promising starting point for more detailed analysis that would take into account the effect of dispersed phase viscosity and holdup. The model was qualitatively supported by limited data from a smaller SMX cartridge (15.75 mm diameter)

5.2 Recommendations for future work

Based on the experience from conducting the experiments, the following suggestions are made to improve the experimental apparatus and the flow visualization/image acquisition system-

- Use of high speed cameras and large aperture zoom lens to get high quality images (without motion blur) with crisp images at high flow rates. This will aid in increasing the recall and precision of the algorithm in these cases
- Inclusion of a recycling line (by means of a 3-way valve) from the separating tank for the continuous phase to avoid manual reloading of the continuous phase tank

Recommendations for further studies are as follows-

- Identification of droplet breakup mechanisms further up the packing-by taking images of its interiors- for different viscosity ratios and surfactant concentrations
- Validations of the influence of the gaps between adjacent plates in the packing, by possibly altering the number of cross bars in its geometry, or by carrying out detailed experiments with different sizes of SMX cartridge.

References

Bentley, B.J., & Leal, L.G. (1986). An experimental investigation of drop deformation and breakup in steady two-dimensional linear flow. *Journal of Fluid Mechanics, **167**,* 241–283.

Berkman, P.D., & Calabrese, R.V. (1988). Dispersion of viscous liquids by turbulent flow in a static mixer. *A.I.Ch.E. Journal, **34**,* 602–609.

Brás, L.M.R., Gomes, E.F., Ribeiro, M.M.M., & Guimarães, M.M.L.(2009). Drop Distribution Determination in a Liquid-Liquid Dispersion by Image Processing. *International Journal of Chemical Engineering*, 746439 -746439.

Bradski, G., & Kaehler, A. (2008). *Learning OpenCV: Computer Vision with the OpenCV*. Sebastopol, CA: O'Reilly Media Inc.

Catalfamo, V., Blum, G.L., & Jaffer, S.A. (2003). *US Patent No. 6,550,960*. Washington, D.C.: U.S. Patent and Trademark Office

Christini, V., Guido, S., Alfani, A., Blawzdziewicz, J., & Lowenberg, M. (2003). Drop breakup and fragment size distribution in shear flow. *Journal of Rheology, **47**,* 1283-1298.

Das, P. K., Legrand, J., Morançais, P., & Carnelle, G. (2005). Drop breakage model in static mixers at low and intermediate Reynolds number. *Chemical Engineering Science,* **60**, 231-238.

De Bruijn, R.A. (1993). Tipstreaming of drops in simple shear flows. *Chemical Engineering Science,* **48**, 277-284.

Fradette, L., Tanguy, P., Li, H.Z., & Choplin, L. (2007). Liquid/Liquid Viscous Dispersions with a SMX Static Mixer. *Chemical Engineering Research and Design, **85**,* 395-405.

Grace, H.P. (1982). Dispersion phenomena in high viscosity immiscible fluid systems and application of static mixers as dispersion devices in such systems. *Chemical Engineering Communications, **14**,* 225–277.

Janssen, J.J.M., Boon, A., & Agterof, W.G.W. (1997). Influence of dynamic interfacial properties on droplet breakup in plane hyperbolic flow. *A.I.Ch.E. Journal, **43**,* 1436–1447.

Karbstein, H., & Schubert, H. (1995). Developments in the continuous mechanical production of oil-in-water macro-emulsions. *Chem.Eng. Proc, **34***: 205–211

Kim, I.G., & Lee, S.Y. (1990). Simple technique for sizing and counting spray drops using digital image processing. *Experimental Thermal and Fluid Science, **3***, 214-221.

Legrand, J., Morançais, P., & Carnelle, G. (2001). Liquid–liquid dispersion in a SMX-Sulzer static mixer. *Chemical Engineering Research & Design, **79***, 949–956.

Liu, S. (2005). *Ph.D. Thesis: Laminar mixing in an SMX static mixer*. Hamilton, ON: McMaster University.

Liu, S.J., Hrymak, A.N., & Wood, P.E. (2005). Drop breakup in an SMX mixer in laminar flow. *Canadian Journal of Chemical Engineering, **83***, 793–807.

Middleman, S. (1974). Drop size distributions produced by turbulent pipe flow of immiscible fluids through a static mixer. *I&EC Process Design and Developments, **13(1)***, 78–83.

Paul, E.L., Atiemo-Obeng, V., & Kresta, S.M. (2004). *Handbook of industrial mixing: Science and Practice*. Hoboken, NJ: John Wiley & Sons Inc.

Mukherjee, P. & Mysels K.J. (1971). *Critical micelle concentration of aqueous surfactant systems*. NSRDS-NBS 36. Washington, D.C.: Office of Standards Reference Data

Rama Rao, N. V., Baird, M. H. I., Hrymak, A. N., & Wood, P. E. (2007). Dispersion of high-viscosity liquid-liquid systems by flow through SMX static mixer elements. *Chemical Engineering Science, **62***, 6885-6896.

Rauline, D., Tanguy, P.A., Le Blevec, J.-M., & Bousquet, J. (1998). Numerical investigation of performance of several static mixers. *Candian Journal of Chemical Engineering, **76***, 527–535.

Streiff, F. (1977). In-line dispersion and mass transfer using static mixing equipment. *Sulzer Technol*, 108.

Streiff, F., Mathys, P., & Fischer, T.U. (1997). New fundamentals for liquid–liquid dispersion using static mixers. *Recents Progrés en Genie des Procedés, **11(51)***, 307–314.

Stone, H.A., & Leal, L.G. (1989). Relaxation and breakup of an initially extended drop in an otherwise quiescent fluid. *Journal of Fluid Mechanics*, ***198***, 399-427.

Thakur, R. K., Vial, C., Nigam, K. D. P., & Nauman, E. B., Djelveh, G. (2003). Static mixers in the process industries: A review. *Chemical Engineering Research and Design*, ***81***, 787-826.

Theron, F., Le Sauze, N., & Ricard, A. (2010). Turbulent Liquid-Liquid Dispersion in Sulzer SMX Mixer. *Ind. Eng. Chem. Res.*, ***49***, 623–632.

Yuen, H.K., Princen, J., Illingworth, J., & Kittler, J. (1990). Comparitive study of Hough Transform methods for circle finding. *Image and vision computing*, ***8***, 71 -7.

Zhang, J., & Pelton, R. (1999). Application of polymer adsorption models to dynamic surface tension. *Langmuir*, ***15***, 5662-5669.

Appendix A

Tabulated Experimental Data

Note: The tabulated data below was used in the Result and Discussion section

Capillary number defined as $\frac{\mu_c u_{cd}}{\sigma}$

Run #	Cell Diameter (m)	No. Elements	μ_c (Pa.S)	μ_d (Pa.S)	p	σ (N/m)	q_c (m^3/sec)	q_d (m^3/sec)	u_{cd} (m/sec)	h	Re_{cd}	Ca	D_{43} (mm)	D_{max} (mm)
1	4.12E-02	10	7.00E-02	4.89E-01	7.0	4.00E-02	1.02E-05	5.00E-06	1.14E-02	0.33	8.66	1.99E-02	3.39	5.44
2	4.12E-02	10	7.00E-02	4.89E-01	7.0	4.00E-02	3.55E-05	6.50E-06	3.15E-02	0.15	23.98	5.52E-02	2.95	5.23
3	4.12E-02	10	7.00E-02	4.89E-01	7.0	4.00E-02	6.83E-05	1.77E-05	6.46E-02	0.21	49.11	1.13E-01	2.36	1.89
4	4.12E-02	10	7.00E-02	4.89E-01	7.0	4.00E-02	1.20E-04	1.30E-05	9.97E-02	0.10	75.85	1.75E-01	1.89	5.58
5	4.12E-02	10	7.00E-02	4.89E-01	7.0	4.00E-02	1.46E-04	3.07E-05	1.33E-01	0.17	100.98	2.32E-01	1.43	4.86
6	1.58E-02	10	7.00E-02	4.89E-01	7.0	4.00E-02	1.03E-05	1.67E-06	6.16E-02	0.14	17.92	1.08E-01	0.99	4.86
7	1.58E-02	10	7.00E-02	4.89E-01	7.0	4.00E-02	1.72E-05	2.33E-06	1.00E-01	0.12	29.11	1.75E-01	0.77	4.86
8	1.58E-02	10	7.00E-02	4.89E-01	7.0	4.00E-02	1.58E-05	2.33E-06	9.32E-02	0.13	27.12	1.63E-01	0.72	4.86
9	4.12E-02	6	7.80E-02	4.89E-01	6.3	4.00E-02	1.13E-05	4.50E-06	1.19E-02	0.28	8.11	2.32E-02	3.85	4.86
10	4.12E-02	6	7.80E-02	4.89E-01	6.3	4.00E-02	3.65E-05	6.50E-06	3.23E-02	0.15	22.04	6.30E-02	3.47	5.44
11	4.12E-02	6	7.80E-02	4.89E-01	6.3	4.00E-02	6.92E-05	1.77E-05	6.52E-02	0.20	44.50	1.27E-01	2.94	5.26
12	4.12E-02	6	7.80E-02	4.89E-01	6.3	4.00E-02	1.22E-04	1.30E-05	1.01E-01	0.10	69.01	1.97E-01	2.43	4.46
13	4.12E-02	6	7.80E-02	4.89E-01	6.3	4.00E-02	1.75E-04	7.83E-06	1.38E-01	0.04	93.87	2.68E-01	2.15	3.82
14	4.12E-02	6	2.50E-02	4.89E-01	19.6	4.00E-02	3.87E-05	1.73E-05	4.20E-02	0.31	89.40	2.62E-02	3.52	5.53
15	4.12E-02	6	2.50E-02	4.89E-01	19.6	4.00E-02	6.32E-05	1.33E-05	5.74E-02	0.17	122.31	3.59E-02	3.50	5.49
16	4.12E-02	6	2.50E-02	4.89E-01	19.6	4.00E-02	8.67E-05	2.33E-05	8.25E-02	0.21	175.74	5.16E-02	3.13	5.25
17	4.12E-02	6	2.50E-02	4.89E-01	19.6	4.00E-02	1.13E-04	1.43E-05	9.59E-02	0.11	204.12	5.99E-02	3.12	4.77
18	4.12E-02	6	2.50E-02	4.89E-01	19.6	4.00E-02	1.42E-04	7.42E-06	1.12E-01	0.05	239.43	7.03E-02	2.89	4.79
19	4.12E-02	10	2.50E-02	4.89E-01	19.6	4.00E-02	3.65E-05	1.77E-05	4.07E-02	0.33	86.61	2.54E-02	3.14	5.23
20	4.12E-02	10	2.50E-02	4.89E-01	19.6	4.00E-02	6.60E-05	1.30E-05	5.93E-02	0.16	126.31	3.71E-02	3.14	5.95
21	4.12E-02	10	2.50E-02	4.89E-01	19.6	4.00E-02	7.30E-05	2.30E-05	7.21E-02	0.24	153.49	4.50E-02	2.89	4.65

Run #	Cell Diameter (m)	No. Elements	μ_c (Pa.S)	μ_d (Pa.S)	p	σ (N/m)	q_c (m^3/sec)	q_d (m^3/sec)	u_{cd} (m/sec)	h	Re_{cd}	Ca	D_{43} (mm)	D_{max} (mm)
22	4.12E-02	10	2.50E-02	4.89E-01	19.6	4.00E-02	1.43E-04	7.67E-06	1.13E-01	0.05	241.43	7.09E-02	2.62	4.11
23	4.12E-02	10	2.50E-02	4.89E-01	19.6	4.00E-02	1.10E-04	1.43E-05	9.34E-02	0.12	198.79	5.83E-02	2.39	4.47
24	4.12E-02	10	2.45E-01	4.89E-01	2.0	4.00E-02	4.74E-05	1.16E-05	4.43E-02	0.20	9.63	2.71E-01	0.89	1.82
25	4.12E-02	10	2.45E-01	4.89E-01	2.0	4.00E-02	4.96E-05	8.25E-06	4.34E-02	0.14	9.44	2.66E-01	0.90	1.75
26	4.12E-02	10	2.45E-01	4.89E-01	2.0	4.00E-02	5.58E-05	3.50E-06	4.45E-02	0.06	9.68	2.73E-01	1.02	1.66
27	4.12E-02	10	2.30E-01	9.78E-01	4.3	4.00E-02	4.57E-05	4.50E-06	3.77E-02	0.09	8.72	2.17E-01	2.07	3.67
28	4.12E-02	10	2.30E-01	9.78E-01	4.3	4.00E-02	6.67E-05	7.83E-06	5.59E-02	0.11	12.95	3.22E-01	1.46	2.80
29	4.12E-02	10	2.30E-01	9.78E-01	4.3	4.00E-02	9.33E-05	1.03E-05	7.78E-02	0.10	18.02	4.48E-01	0.94	1.89
31	4.12E-02	10	2.30E-01	9.78E-01	4.3	4.00E-02	1.18E-04	1.16E-05	9.70E-02	0.09	22.46	5.58E-01	0.69	1.31
32	4.12E-02	10	7.80E-02	9.78E-01	12.5	4.00E-02	8.23E-05	3.83E-06	6.47E-02	0.04	44.16	1.26E-01	2.52	4.23
33	4.12E-02	10	7.80E-02	9.78E-01	12.5	4.00E-02	7.50E-05	8.33E-06	6.26E-02	0.10	42.71	1.22E-01	2.41	4.03
34	4.12E-02	10	7.80E-02	9.78E-01	12.5	4.00E-02	7.30E-05	1.30E-05	6.46E-02	0.15	44.07	1.26E-01	2.25	4.30
35	4.12E-02	10	7.80E-02	9.78E-01	12.5	4.00E-02	6.92E-05	1.63E-05	6.42E-02	0.19	43.82	1.25E-01	2.25	3.53
36	4.12E-02	10	7.80E-02	9.78E-01	12.5	4.00E-02	1.04E-04	1.10E-05	8.61E-02	0.10	58.76	1.68E-01	2.10	3.94
37	4.12E-02	10	7.80E-02	9.78E-01	12.5	4.00E-02	1.36E-04	1.43E-05	1.13E-01	0.10	76.91	2.20E-01	1.73	3.44
38	4.12E-02	10	7.80E-02	9.78E-01	12.5	4.00E-02	3.67E-05	3.83E-06	3.04E-02	0.09	20.75	5.93E-02	3.20	5.55
39	4.12E-02	10	2.70E-02	9.78E-01	36.2	4.00E-02	5.33E-05	6.50E-06	4.49E-02	0.11	88.58	3.03E-02	3.63	5.58
40	4.12E-02	10	2.70E-02	9.78E-01	36.2	4.00E-02	7.77E-05	8.83E-06	6.49E-02	0.10	128.06	4.38E-02	3.30	5.38
41	4.12E-02	10	2.70E-02	9.78E-01	36.2	4.00E-02	1.02E-04	1.20E-05	8.53E-02	0.11	168.28	5.76E-02	3.06	4.61
42	4.12E-02	10	2.70E-02	9.78E-01	36.2	4.00E-02	1.30E-04	1.48E-05	1.09E-01	0.10	214.42	7.34E-02	2.65	4.20
43	4.12E-02	10	2.70E-02	9.78E-01	36.2	4.00E-02	6.67E-05	1.77E-05	6.33E-02	0.21	124.85	4.27E-02	3.20	5.58
44	4.12E-02	10	2.70E-02	9.78E-01	36.2	2.30E-02	5.67E-05	6.50E-06	4.74E-02	0.10	93.51	5.57E-02	3.39	4.84
45	4.12E-02	10	2.70E-02	9.78E-01	36.2	2.30E-02	9.58E-05	8.83E-06	7.86E-02	0.08	154.95	9.23E-02	2.90	4.28

Run #	Cell Diameter (m)	No. Elements	μ_c (Pa.S)	μ_d (Pa.S)	p	σ (N/m)	q_c (m^3/sec)	q_d (m^3/sec)	u_{cd} (m/sec)	h	Re_{cd}	Ca	D_{43} (mm)	D_{max} (mm)
46	4.12E-02	10	2.70E-02	9.78E-01	36.2	2.30E-02	1.15E-04	1.15E-05	9.50E-02	0.09	187.28	1.11E-01	2.60	4.87
47	4.12E-02	10	2.70E-02	9.78E-01	36.2	2.30E-02	1.41E-04	1.50E-05	1.17E-01	0.10	230.70	1.37E-01	2.30	4.41
48	4.12E-02	10	2.70E-02	9.78E-01	36.2	2.30E-02	6.13E-05	6.50E-06	5.09E-02	0.10	100.42	5.98E-02	3.19	4.72
49	4.12E-02	10	2.70E-02	9.78E-01	36.2	2.30E-02	2.50E-05	6.50E-06	2.37E-02	0.21	46.63	2.78E-02	3.37	4.86
53	4.12E-02	10	2.70E-02	4.89E-01	18.1	2.30E-02	2.50E-05	5.00E-06	2.25E-02	0.17	44.41	2.64E-02	3.41	5.09
54	4.12E-02	10	2.70E-02	4.89E-01	18.1	2.30E-02	1.13E-04	1.30E-05	9.49E-02	0.10	187.03	1.11E-01	2.18	4.13
55	4.12E-02	10	2.70E-02	4.89E-01	18.1	2.30E-02	8.50E-05	8.83E-06	7.05E-02	0.09	138.91	8.27E-02	2.60	4.41
56	4.12E-02	10	2.70E-02	4.89E-01	18.1	2.30E-02	1.48E-04	1.63E-05	1.24E-01	0.10	243.78	1.45E-01	1.88	3.57
57	4.12E-02	10	2.70E-02	4.89E-01	18.1	2.30E-02	5.83E-05	6.50E-06	4.87E-02	0.10	95.98	5.71E-02	2.92	5.09
58	4.12E-02	10	2.70E-02	4.89E-01	18.1	2.30E-02	9.00E-05	4.17E-06	7.07E-02	0.04	139.41	8.30E-02	2.38	4.31
59	4.12E-02	10	2.70E-02	4.89E-01	18.1	2.30E-02	7.67E-05	1.50E-05	6.88E-02	0.16	135.71	8.08E-02	2.70	4.72
60	4.12E-02	10	7.40E-02	4.89E-01	6.6	2.30E-02	6.68E-05	6.50E-06	5.51E-02	0.09	39.61	1.77E-01	2.12	3.88
61	4.12E-02	10	7.40E-02	4.89E-01	6.6	2.30E-02	3.05E-05	3.33E-06	2.54E-02	0.10	18.28	8.17E-02	2.57	4.53
62	4.12E-02	10	7.40E-02	4.89E-01	6.6	2.30E-02	1.02E-04	1.00E-05	8.38E-02	0.09	60.32	2.70E-01	1.54	3.18
64	4.12E-02	10	7.40E-02	4.89E-01	6.6	2.30E-02	1.43E-04	1.53E-05	1.19E-01	0.10	85.71	3.83E-01	1.12	2.33
65	4.12E-02	6	7.40E-02	4.89E-01	6.6	2.30E-02	1.02E-04	1.12E-05	8.47E-02	0.10	60.95	2.73E-01	1.89	3.29
66	4.12E-02	6	7.40E-02	4.89E-01	6.6	2.30E-02	1.37E-04	1.50E-05	1.14E-01	0.10	81.92	3.66E-01	1.46	3.01
67	4.12E-02	6	7.40E-02	4.89E-01	6.6	2.30E-02	6.00E-05	7.67E-06	5.08E-02	0.11	36.55	1.63E-01	2.85	4.97
68	4.12E-02	6	7.40E-02	4.89E-01	6.6	2.30E-02	2.83E-05	3.33E-06	2.38E-02	0.11	17.11	7.65E-02	3.41	5.21
69	4.12E-02	6	7.40E-02	4.89E-01	6.6	2.30E-02	7.75E-05	8.33E-06	6.44E-02	0.10	46.36	2.07E-01	2.65	4.66
71	4.12E-02	10	7.40E-02	9.78E-01	13.2	2.30E-02	3.28E-05	3.58E-06	2.73E-02	0.10	19.67	8.80E-02	3.21	5.37
72	4.12E-02	10	7.40E-02	9.78E-01	13.2	2.30E-02	6.27E-05	7.42E-06	5.26E-02	0.11	37.86	1.69E-01	2.67	4.78
73	4.12E-02	10	7.40E-02	9.78E-01	13.2	2.30E-02	8.03E-05	8.67E-06	6.68E-02	0.10	48.07	2.15E-01	2.52	4.32

Run #	Cell Diameter (m)	No. Elements	μ_c (Pa.S)	μ_d (Pa.S)	p	σ (N/m)	q_c (m^3/sec)	q_d (m^3/sec)	u_{cd} (m/sec)	h	Re_{cd}	Ca	D_{43} (mm)	D_{max} (mm)
74	4.12E-02	10	7.40E-02	9.78E-01	13.2	2.30E-02	1.49E-04	1.43E-05	1.23E-01	0.09	88.32	3.95E-01	2.18	4.08
75	4.12E-02	10	7.40E-02	9.78E-01	13.2	2.30E-02	1.03E-04	1.30E-05	8.68E-02	0.11	62.48	2.79E-01	2.27	4.11
76	4.12E-02	10	7.40E-02	9.78E-01	13.2	2.30E-02	1.34E-04	1.38E-05	1.11E-01	0.09	79.58	3.56E-01	2.27	4.06
77	4.12E-02	10	2.30E-01	9.78E-01	4.3	2.30E-02	4.57E-05	4.50E-06	3.77E-02	0.09	8.72	3.77E-01	1.78	3.30
78	4.12E-02	10	2.30E-01	9.78E-01	4.3	2.30E-02	7.30E-05	7.67E-06	6.06E-02	0.10	14.02	6.06E-01	1.16	2.29
79	4.12E-02	10	2.30E-01	9.78E-01	4.3	2.30E-02	9.69E-05	1.00E-05	8.03E-02	0.09	18.58	8.03E-01	0.82	1.86
80	4.12E-02	10	2.30E-01	9.78E-01	4.3	2.30E-02	1.14E-04	1.30E-05	9.52E-02	0.10	22.04	9.52E-01	0.61	1.44
81	4.12E-02	10	2.30E-01	9.78E-01	4.3	2.30E-02	2.83E-05	3.33E-06	2.38E-02	0.11	5.50	2.38E-01	1.97	3.55
82	4.12E-02	10	2.30E-01	9.78E-01	4.3	1.30E-02	2.89E-05	3.58E-06	2.44E-02	0.11	5.65	4.32E-01	1.55	3.17
83	4.12E-02	10	2.30E-01	9.78E-01	4.3	1.30E-02	4.83E-05	5.00E-06	4.00E-02	0.09	9.27	7.08E-01	1.27	2.42
84	4.12E-02	10	2.30E-01	9.78E-01	4.3	1.30E-02	7.00E-05	7.17E-06	5.79E-02	0.09	13.41	1.03E+00	0.76	1.47
85	4.12E-02	10	2.30E-01	9.78E-01	4.3	1.30E-02	9.50E-05	6.50E-06	7.62E-02	0.06	17.64	1.35E+00	0.44	0.85
87	4.12E-02	10	6.00E-02	9.78E-01	16.3	1.30E-02	2.17E-05	3.33E-06	1.88E-02	0.13	16.65	8.66E-02	2.45	4.10
88	4.12E-02	10	6.00E-02	9.78E-01	16.3	1.30E-02	7.11E-05	8.83E-06	6.00E-02	0.11	53.24	2.77E-01	2.00	3.89
89	4.12E-02	10	6.00E-02	9.78E-01	16.3	1.30E-02	4.87E-05	5.00E-06	4.03E-02	0.09	35.75	1.86E-01	2.20	3.85
91	4.12E-02	10	6.00E-02	9.78E-01	16.3	1.30E-02	1.01E-04	1.15E-05	8.41E-02	0.10	74.61	3.88E-01	1.97	3.74
92	4.12E-02	10	6.00E-02	9.78E-01	16.3	1.30E-02	1.27E-04	1.43E-05	1.06E-01	0.10	93.93	4.89E-01	1.37	2.65
93	4.12E-02	10	6.00E-02	4.89E-01	8.2	1.30E-02	2.50E-05	3.58E-06	2.15E-02	0.13	19.04	9.91E-02	2.33	4.06
94	4.12E-02	10	6.00E-02	4.89E-01	8.2	1.30E-02	4.99E-05	7.17E-06	4.29E-02	0.13	38.03	1.98E-01	1.87	3.47
95	4.12E-02	10	6.00E-02	4.89E-01	8.2	1.30E-02	7.17E-05	7.08E-06	5.91E-02	0.09	52.46	2.73E-01	1.67	2.90
96	4.12E-02	10	6.00E-02	4.89E-01	8.2	1.30E-02	1.01E-04	1.16E-05	8.42E-02	0.10	74.67	3.88E-01	1.50	2.55

Appendix B

Code in Visual C++ with OpenCV library

```
//The following code was used for image processing and has been
explained in the experimental section (section 3.4)

#include "stdafx.h"


#include <cv.h>
#include <cxcore.h>
#include <highgui.h>
#include <math.h>
#include <sstream>
#include <iostream>
#include <fstream>
#include <stdio.h>
#include <stdlib.h>

using namespace std;

cvHoughCircles_2( CvArr* src_image, void* circle_storage,
                int method, double dp, double min_dist,
                double param1, double param2,
                int min_radius, int max_radius, int circles_max );

int _tmain(int argc, _TCHAR* argv[])
{
            IplImage *image,*e,*contour;
            const char *c_filename, *c_filename_output;
            string filename, filename_output;
            string
string1="run87/run87_0",string2="_output",string3="run87/run87_000
",string4="run87/run87_00";

            int frame;
            string s;
            stringstream out;
            ofstream myfile;

            //output file for radius vector
            myfile.open("run87/output_run87.txt");

            for(frame=1; frame<=200; frame++)
            {

            out<<frame;
            s=out.str();
            if(frame<10){

                  filename=string3+s+".bmp";
            }
            else if(frame<=99){
                  filename=string4+s+".bmp";
            }
            else {
                  filename=string1+s+".bmp";
```

```
            }

            c_filename=filename.c_str();


            image =
cvLoadImage(c_filename,CV_LOAD_IMAGE_GRAYSCALE);
            e = cvCloneImage(image);



            //bilateral smoothing
            cvSmooth(image,e,CV_BILATERAL,11,11,100,5);

            cvWaitKey(0);
            CvMemStorage* storage = cvCreateMemStorage(0);

            //Hough transform for small radii
            CvSeq* results1 = cvHoughCircles_2(e,

      storage,

      CV_HOUGH_GRADIENT,
                                                      2,
                                                      100,
                                                      22,
                                                      150,
                                                      18,
                                                      99,

      12);//threshold was 75//Canny for big mixer was 40//

            //Hough transform for large radii
            CvSeq* results2 = cvHoughCircles_2(e,

      storage,

      CV_HOUGH_GRADIENT,
                                                      2,
                                                      150,
                                                      22,
                                                      220,
                                                      100,
                                                      310,

      10);//thershold was 160//Canny for big mixer was 50*/

            //output results in the text file and mark indentifed
circles
            for( int i = 0; i < results1->total; i++ ) {
                  float* p = (float*) cvGetSeqElem( results1, i );
                  CvPoint pt = cvPoint( cvRound( p[0] ), cvRound(
            p[1] ) );
                  myfile<<cvRound(p[2])<<"\n";
```

```
                cvCircle(
                            image,
                            pt,
                            cvRound( p[2] ),
                            CV_RGB(0xff,0xff,0xff),
                            6
                            );
                }

          for( int i = 0; i < results2->total; i++ ) {
                float* p = (float*) cvGetSeqElem( results2, i );
                CvPoint pt = cvPoint( cvRound( p[0] ), cvRound(
          p[1] ) );
                myfile<<cvRound(p[2])<<"\n";
                cvCircle(
                            image,
                            pt,
                            cvRound( p[2] ),
                            CV_RGB(0xff,0xff,0xff),
                            6
                            );
          }



          filename_output=string1+s+string2+".jpg";

          c_filename_output=filename_output.c_str();
          cvSaveImage(c_filename_output,image);

          cvReleaseImage(&image);
          cvReleaseImage(&e);
          s.clear();
          out.str(string());
}
myfile.close();
}
```